TU Delft

In silico screening of Ruthenium pincer complexes for Liquid Organic Hydrogen Carrier (LOHC) applications

Lotte Vonck

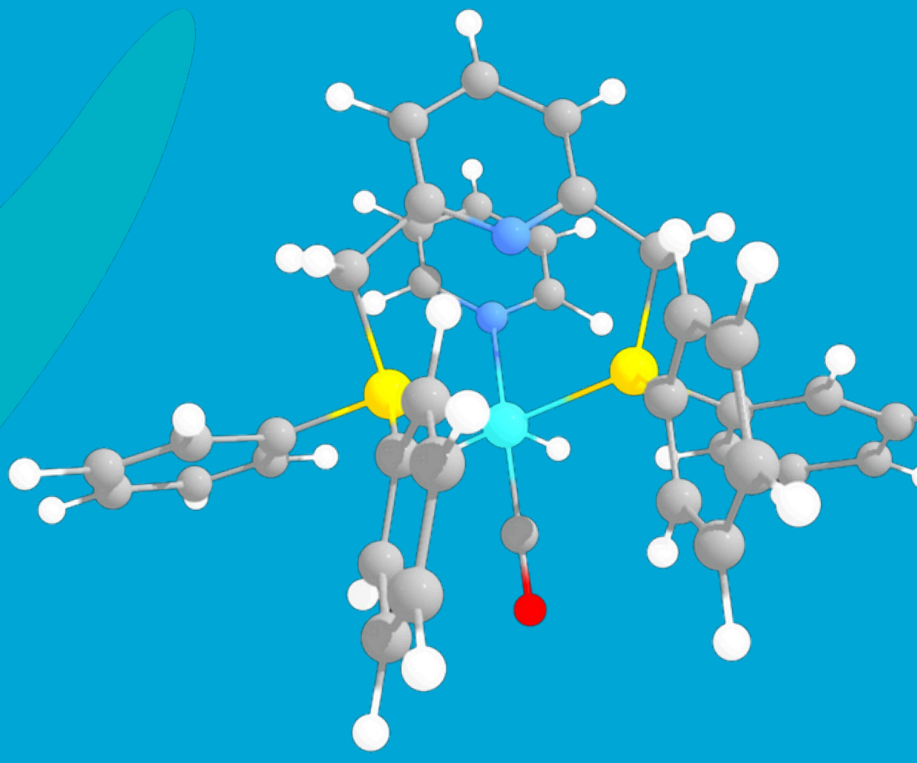

In silico screening of Ruthenium pincer complexes for Liquid Organic Hydrogen Carrier (LOHC) applications

by

Lotte Vonck

to obtain the degree of Bachelor of Science
at the Delft University of Technology.

Performed at:
Inorganic Systems Engineering
Chemical Engineering
Faculty of Applied Sciences

Under supervision of:
Prof. Dr. E. A. Pidko
PhD(c). A. Kalikadien
Dr. A. A. Kolganov

Student number:	5170427 / s2639416
Project duration:	April 22, 2025 – July 22, 2025
Thesis committee:	Prof. Dr. E. A. Pidko, TU Delft, supervisor
	Prof. Dr. T. Bouwens, TU Delft
	Dr. A. A. Kolganov, TU Delft

TU Delft Delft University of Technology

ISEgroup ChemE @ TU Delft

Abstract

This work presents a high-throughput *in silico* screening of ruthenium(II) pincer complexes as potential catalysts for pyridine hydrogenation To explore how backbone architecture, substituent sterics, and hemilability govern substrate binding energetics, this study screened 24 Ru(II) pincer complexes comprising four distinct lutidine-based pincer backbones (PNpyP, PONpyOP, NONpyON, NNpyN) and six substituents (Me, iPr, tBu, Bu, Ph, Cy). Additionally, 18 complexes representing three specific coordination modes from the PNpyP ligand family were screened using pyridine as a model substrate.

MACE was employed to generate stereoisomer and conformer libraries without conformational bias. Structures were screened with the Universal Force Field, refined via DFT (PBE0-D3(BJ)/def2-SVP), and analysed using ensemble-averaged steric descriptors (percent buried volume and bite angle) and pyridine binding free energies across three coordination pathways: (i) carbonyl auxiliary substitution, (ii) central nitrogen donor dissociation, and (iii) phosphorus side-arm dissociation.

The results reveal that pyridine binding to form RuH_2(py)(κ^3-PNP), RuH_2(CO)(κ^2-P,N-PNP)(py), or RuH_2(CO)(κ^2-P,P-PNP)(py) complexes is generally unfavorable. However, binding becomes more accessible via the hemilabile dissociation of either the nitrogen or phosphorus pincer donor. Dissociation of the nitrogen donor emerged as the most energetically accessible pathway (ΔG = 30–105 kJ/mol), particularly with phenyl substituents where π–π stacking stabilises binding (ΔG = 29.9 kJ/mol). Conversely, dissociation of the phosphorus pincer donor (ΔG = 60–105 kJ/mol) presents the most favorable binding energetics in the presence of bulky substituents, as the enhanced flexibility of the phosphine side-arm accommodates steric bulk more effectively. Substitution of the carbonyl remains largely inaccessible (ΔG = 100–150 kJ/mol), as it requires the coordination of pyridine to a fully occupied complex.

Analysis of the ensemble-averaged steric descriptors revealed that an optimal balance between ligand hemilability, steric constraints, and geometric flexibility governs substrate accessibility. A percent buried volume in the range of 40–50% and P–Ru–P bite angles near 95–115° showed significantly improved pyridine binding energetics. This was exemplified by the RuH_2(CO)(κ^2-P,P-PNP)(py) complex, where structural reorganisation upon nitrogen dissociation allows the complex to exploit conformational flexibility and stabilise substrate binding through non-covalent interactions. This creates a confined, well-defined pocket adjacent to the metal center that effectively accommodates the substrate. These findings warrant further investigation to bridge computational insights with improved catalytic performance.

Contents

1

Introduction

Central to the global effort of decarbonization is the fundamental reimagination of its energy vectors, which requires not only replacing fossil resources but also fundamentally rethinking how energy is stored, transported, and transformed in chemical form. In this paradigm, *N*-heterocycles such as substituted pyridines, functioning as liquid organic hydrogen carriers (LOHCs), offer a potentially transformative approach [1–5].

Homogeneous pincer complexes sit at the core of many catalytic strategies for hydrogen storage, CO_2 utilisation activity and selectivity. Among transition metals used in this context, the noble metal ruthenium (Ru) occupies a central position. Compared with other 3*d* metals, Ru pincer complexes tend to exhibit higher intrinsic reactivity and robustness, which enables lower catalyst loadings, extended lifetimes, and more straightforward recycling, key attributes for sustainable homogeneous catalysis [3, 6–9].

Ru-based pincer catalysts form a broad and versatile platform. Ligand frameworks such as PNP, PNN, CNC, and PN_3P facilitate metal–ligand cooperative activation of small molecules (H_2, CO_2), enabling reversible LOHC transformations. Within this family, lutidine-derived PNP and CNC pincers have set performance benchmarks for CO_2 hydrogenation to formate. Through careful steric and electronic tuning, these pincer systems achieve exceptional efficiencies at minimal Ru loadings. For instance, work by Filonenko, Pidko, and co-workers on Ru–PNP families has demonstrated TOFs on the order of 10^6 h^{-1} and TONs above 10^5 in reversible cycles, rivalling systems based on other noble metals such as iridium [7–10].

Recent advances in computational chemistry have created new possibilities to enumerate stereoisomers and conformers of ruthenium pincer complexes at scale. Automated computational workflows, such as MACE, offer a route to couple high-throughput conformer sampling with quantum-chemical refinement and statistical analysis. However, these tools are seldom combined with ensemble-averaged steric descriptors or with thermodynamic measures of hemilability, such as the free energies associated with donor-arm dissociation and substrate substitution, within a single, unified protocol. As a result, current design rules for Ru-pincer catalysts often remain tied to specific case studies that do not fully exploit the conformational flexibility and hemilabile behaviour encoded in the ligand architecture [11–13].

These advances illustrate a broader conceptual point: although Ru is a noble metal, its combination of high activity, stability under turnover, and compatibility with low loading and recycling can render Ru pincer catalysts highly attractive from a practical sustainability standpoint, particularly when contrasted with less active base-metal analogues that require harsher conditions or higher loadings. Despite extensive mechanistic and kinetic studies, the complex interplay between pincer backbone architecture, substituent bulk, and conformational dynamics to substrate binding and catalytic performance remain only partially quantified [14–18].

This study addresses this gap by utilising a unified computational workflow that integrates automated structure generation, universal force field and density functional theory refinement, and ensemble-based statistical analysis for lutidine-derived Ru pincer complexes. MACE is employed to generate comprehensive stereoisomeric and conformational bias-free libraries across diverse pincer backbones (PNP, PONOP, NONON, NNN) and substituents. An initial screening using the Universal Force Field (UFF) identified low-energy conformational candidates from these libraries. Subsequent geometry optimisation and thermochemical calculations were performed at the PBE0-D3(BJ)/def2-SVP level of theory using the ORCA software package. Hemilability is quantified through defined pyridine coordination pathways, carbonyl auxiliary ligand substitution, and competitive dissociation of nitrogen or phosphorus pincer donors, and their associated binding free energies. Concurrently, ensemble-averaged steric descriptors were computed on the DFT-optimised structures to correlate the local environment with substrate binding thermodynamics [13, 19, 20].

2

Theoretical background

The background information outlined in this chapter establishes the theoretical framework essential for understanding the results presented and discussed throughout this thesis. Section 2.1 offers an overview of the molecular descriptors employed in this study. The chapter concludes with an introduction to the Boltzmann average as a framework for analysing conformational ensembles.

2.1 Descriptors

Molecular descriptors are one of the pillars of predictive catalyst design. They quantify catalyst properties, enabling the correlation of experimental behaviour with molecular structure. In computational modelling of homogeneous catalysis, these descriptors encode complex electronic and steric features into numerical variables suitable for quantitative analysis. This study focuses on steric descriptors, specifically buried volume and bite angle, which describe the spatial properties of ligands, as discussed below [21].

2.1.1 Buried Volume

The buried volume ($\%V_{bur}$) is a steric descriptor for modulating the steric environment conferred on a metal by a ligand. This term is defined as the percentage of the total volume of a sphere, with a radius of R, occupied by a ligand at a given metal–ligand bond distance (Figure 2.1) [22].

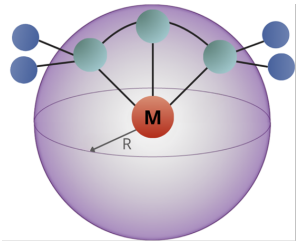

Figure 2.1: Schematic representation of the percent buried volume ($\%V_{bur}$) of a pincer ligand.

To calculate the percent buried volume, the metal centre M must be defined first. In a transition metal complex with a pincer ligand, such as a PNP-type ligand, the ligand coordinates through two phosphorus atoms and a central nitrogen atom. The metal centre M is typically the actual metal atom in the structure. Its position lies along the line passing through the central coordinating atom, such as the nitrogen atom, and the centre of mass of the selected coordinating atoms of the pincer ligand. Once M is defined, a sphere of radius R is constructed around it [22].

This sphere is partitioned using a regular 3D cubic mesh with spacing s, resulting in cubic voxels V_{xyz}, each with a volume of s^3. For each voxel, the distance from its center to every atom in the ligand is measured. If no ligand atom lies within a van der Waals contact distance of the voxel's centre, its volume (s^3) is added to the free volume V_{Free}. Conversely, if at least one ligand atom is within a van der Waals contact distance, the voxel is classified as occupied. In other words, an occupied voxel represents a region sterically hindered by the ligand, and its volume is added to the buried volume V_{Bur}. This voxel-based classification leads to the following equation [22]:

$$V_{\text{Sphere}} = \sum V_{xyz} = V_{\text{Free}} + V_{\text{Bur}} = \sum V_{xyz}(\text{Free}) + \sum V_{xyz}(\text{Buried}) \tag{2.1}$$

Building upon equation 2.1, the final expression for the percentage of the sphere's volume that is buried under the van der Waals radii of surrounding atoms [22]:

$$\%V_{\text{Bur}} = 100 \cdot \frac{V_{\text{Bur}}}{V_{\text{Sphere}}} \tag{2.2}$$

In this study, Buried Volume is computed using the SEQCROW plugin bundle for UCSF ChimeraX [23], as described in the methodology section.

2.1.2 Bite Angle

Bite angle is a steric descriptor used to describe the angle between two donor atoms and the metal centre (Figure 2.2). This descriptor measures the net interaction with the metal centre, capturing a mixture of steric and electronic effects. In the case of chelating ligands, it measures the geometric constraints imposed by the backbone of chelating ligands, which can limit the proximity of the donor groups to the metal. As a result, chelating ligands may bind with bite angles that are significantly larger or smaller than the ideal geometrical value, thereby impacting the ground state or transition state of metal complexes involved in a chemical reaction [24].

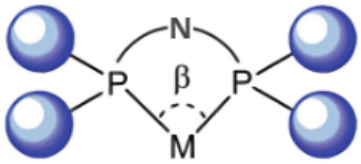

Figure 2.2: Schematic representation of the bite angle (β) in a pincer metal complex.

Pincer ligands are a class of chelating ligands that coordinate to the metal centre through three donor atoms in a meridional arrangement. The P–Ru–P bite angle of the pincer metal complex provides insight into the geometric constraints imposed by the ligand framework [24].

Bite angles were determined based on the Cartesian coordinates derived from optimised geometries obtained through ORCA 6.0.1 calculations [25]. For this calculation a custom Python script was employed, as detailed in the methodology section 3.2.5.

2.2 Boltzmann Average

The Boltzmann average, $\langle A \rangle$ is defined as the thermodynamic ensemble average of an observable A, computed as a weighted mean over a set of chemical conformers. The weights are given by the Boltzmann factor e^{-E_i/k_BT} where E_i represents the internal energy of conformer i, k_B is Boltzmann's constant, and T is the absolute temperature, sufficiently high to justify the neglect of quantum mechanical effects. Mathematically, the Boltzmann average is expressed as:

$$\langle A \rangle = \frac{\sum_i A_i e^{-E_i/k_BT}}{\sum_i e^{-E_i/k_BT}} \tag{2.3}$$

where the summations run over all conformers considered [26, 27].

3

Methodology

3.1 Metal Complexes Embedding (MACE)

Initial 3D structures were generated using the Metal Complexes Embedding (MACE) pipeline, a Python tool that automates the creation of all feasible stereoisomers and 3D geometries for mono-nuclear octahedral and square-planar transition metal complexes from SMILES strings. It operates without user intervention, ensuring unbiased structure generation based on input parameters: metal type, geometry, and ligand SMILES with atom mappings [11].

MACE enumerates all possible donor atom arrangements, then filters out duplicates using RDKit's canonicalization (USMILES), and removes high-energy or chemically implausible structures via sub-structure pattern recognition. It constructs 3D coordinates through RDKit's distance geometry, applying custom bounds for metal–donor distances, and refines geometries using an extended Universal Force Field (UFF). Final structures are output as XYZ files, which contain the 3D coordinates of each atom [11].

High-throughput hemilability exploration

MACE provides a systematic approach to challenge and expand beyond initial assumptions in coordination chemistry. A common assumption in the field is that pincer ligands fully coordinate to a metal centre via all three donor atoms. However, MACE enables the exploration of scenarios where coordination can be manually reduced by specifying only two out of three donor centres on a pincer ligand as the coordinating sites. By automating configuration generation, MACE can first model the fully coordinated pincer ligand complex and then systematically examine intermediate states where one or even two donor atoms remain bound to the metal centre. Vacated donor sites in these reduced coordination scenarios can be replaced with a model substrate. This process enables the computational evaluation of intermediate coordination configurations that might otherwise be overlooked in traditional experimental approaches, making it a computationally efficient method to study hemiability [11].

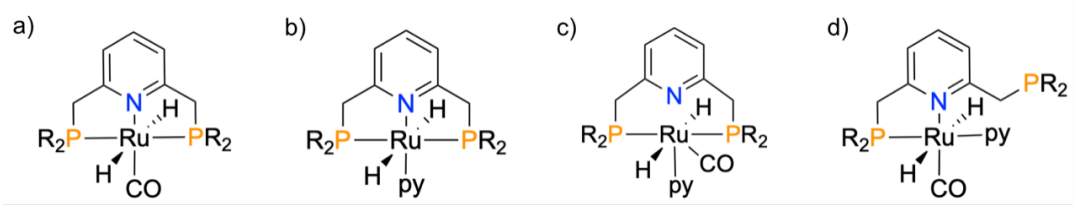

Figure 3.1: Schematic of Ruthenium pincer complex (isomer 0), featuring trans coordination of hydrides and the carbonyl ligand positioned trans to the nitrogen atom of the lutidine backbone. (a) $RuH_2(CO)(\kappa^3\text{-PNP})$; (b) CO replaced by pyridine, $RuH_2(py)(\kappa^3\text{-PNP})$; (c) N-donor displaced, $RuH_2(CO)(\kappa^2\text{-P,P-PNP})(py)$; (d) P-donor arm displaced by pyridine, $RuH_2(CO)(\kappa^2\text{-P,N-PNP})(py)$.

To study the principal possibility of the pincer donor hemilability, the $RuH_2(CO)(\kappa^3\text{-PNP})$ pincer complex is considered as a model system, with a PNP pincer ligand, ruthenium metal centre, and a carbonyl and two hydrides as auxiliary ligands (Figure 3.1a).

The starting definition of the $RuH_2(CO)(\kappa^3\text{-PNP})$ complex components has been modified by introducing pyridine as a model substrate and specifying only two out of three donor centres on the $R_2P–N–PR_2$ pincer as the coordinating sites, enabling the generation of three substrate-specific complexes (Figure 3.1b–d). Three situations were considered (Figure 3.2): (i) substitution of the carbonyl auxiliary ligand by pyridine; (ii) the central donor atom N of the pincer backbone dissociates and pyridine coordinates; (iii) the side-arm PR_2 of the pincer backbone dissociates and pyridine coordinates.

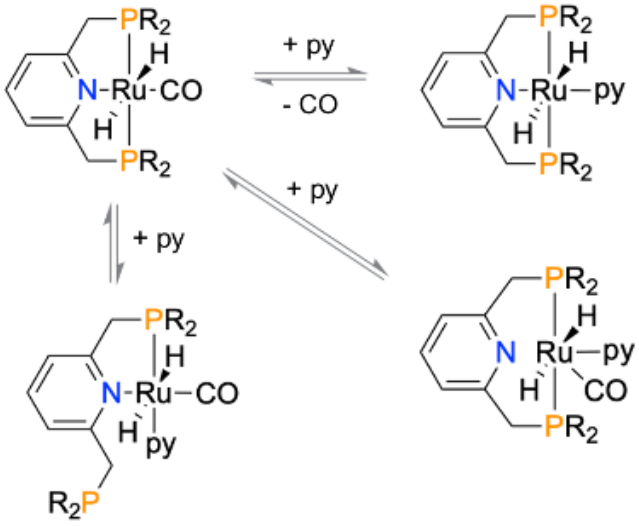

Figure 3.2: Pathways and associated configurations of hemilabile equilibria exemplified on RuPNP pincer complexes.

To quantify hemilability, the binding energy of pyridine, used as a model substrate, is computed for each pathway as a quantitative descriptor to predict the catalytic performance of these substitutions.

The pyridine binding free energy, $\Delta G_{\text{binding}}$, is defined by the general reaction:

$$\Delta G_{\text{binding}} = G_{\text{complex with pyridine}} - G_{\text{complex}} - G_{\text{pyridine}} + G_{\text{dissociated ligand}}, \tag{3.1}$$

where:

- $G_{\text{complex with pyridine}}$ is the Gibbs free energy of the metal complex with coordinated pyridine,
- G_{complex} is the Gibbs free energy of the starting complex,
- G_{pyridine} is the Gibbs free energy of free pyridine,
- $G_{\text{dissociated ligand}}$ is the Gibbs free energy of the ligand displaced upon pyridine binding.

All energy values are derived from DFT calculations conducted under standard conditions at 298.15 K and 1 atm, discussed in Section 3.2.3.

3.2 Computational workflow

The computational workflow used in this study is depicted in Figure 3.3. In the subsequent sections, the workflow steps are discussed, followed by specific computational chemistry details.

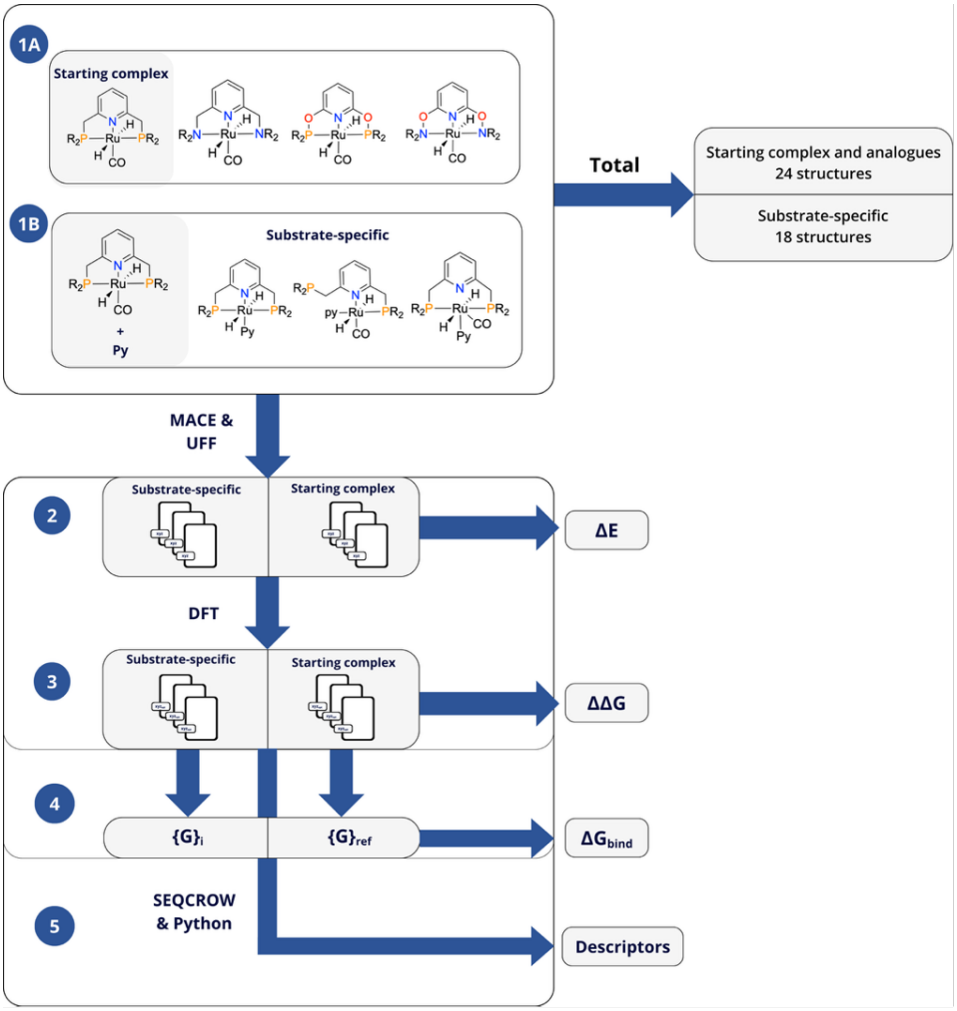

Figure 3.3: Summary of the computational workflow applied in this study.

3.2.1 Ligand library

A comprehensive catalytic database was constructed to facilitate the generation of the complexes depicted in Figure 3.1. This database encompasses Ruthenium (II) singlet-state complexes coordinated with NNN, NONON, and PONOP- or PNP-type pincer ligands, all anchored to a 2,6-lutidine scaffold (Figure 3.4b).

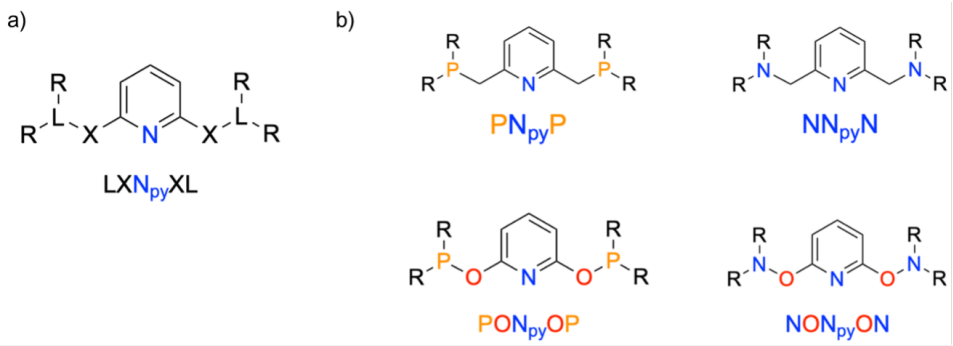

Figure 3.4: Explored chemical space of the reference structure. (a) Initialisation strategy for Ru lutidine-based pincers with R_i = {Me, Bu, tBu, iPr, Cy, Ph}; ligand set L = {N, P}; X = {O, CH_2}. (b) Pincer ligand architectures

The donor atom (L) is nitrogen (–NR_2) or phosphorus (–PR_2), forming L–X–Npy–X–L side-arm architectures, where X denotes the backbone linker, either oxygen (O) or methylene (CH_2), connecting the central nitrogen donor to the outer L donors (Figure 7a). Six alkyl and aryl substituents (R) were evaluated on the donor atoms to assess their effect on the binding preference of the incoming model substrate: methyl (Me), isopropyl (iPr), tert-butyl (tBu), n-butyl (Bu), phenyl (Ph), and cyclohexyl (Cy).

Systematic variation of both the donor atom (L = N or P), the linker (X = O or CH_2), and the substituent (R) facilitates a detailed assessment of steric and electronic effects on substrate coordination within a structurally consistent ligand framework.

The database derived from the ligand framework variations labelled as LXNpyXL comprises 4 distinct ligand backbone frameworks: PNpyP, NNpyN, PONpyOP, NONpyON. Systematic donor group substitutions are implemented on the side-arm X using the representative set of substituents R.

3.2.2 MACE command-line interface

To generate the structures (as shown in workflow steps 1A and 1B, Figure 3.3), the MACE software's command-line interface (CLI) was used. The MACE workflow was initiated by using the `epic-mace-quickstart` command, which created the template input files: `mace_input.yaml` and `substituents.yaml`. The `mace_input.yaml` file defines the complex's structure using SMILES notation, geometry, stereomer search rules, and parameters for conformer generation and filtering. The `substituents.yaml` file maps substituent names to their SMILES definitions, each including a dummy atom for attachment to the core scaffold [28].

The `mace_input.yaml` file was then modified using extended SMILES to specify the building blocks of the complex: the pincer ligand, the ruthenium metal centre, and the auxiliary ligands (two hydrides and a carbonyl). The geometry was set to octahedral, and each donor atom was labelled with atomic map numbers (1–6) corresponding to octahedral coordination. Variations in donor atoms at these positions, defined as pincer ligands with S (sulfur), N (nitrogen), or P (phosphorus) donors, generated different backbones: NNN, PNN, PNP, and SNS.

A placeholder approach was used to further define the scaffold. The R labels on the phosphorus donor atoms (Figure 3.4a) were attached through dummy atoms to the core scaffold. The MACE software combinatorially generated structures by replacing these dummy atoms with substituents (H, Me, iPr, tBu, Bu, Ph, Cy) defined in the `substituents.yaml` file. This enabled the systematic generation of the structures in step 1A, as illustrated in Figure 3.3.

The substrate-specific structures (step 1B) were manually constructed by modifying the `mace_input.yaml` file. For the RuH_2(py)(κ^3-PNP) complex, the auxiliary carbonyl ligand was replaced with pyridine by updating the SMILES notation. For the RuH_2(CO)(κ^2-P,N-PNP)(py) complex, only two of the three donor centres on the PNP pincer ligand were specified as coordinating sites, displacing the phosphorus donor atom. The same approach was applied to displace the central nitrogen atom in the RuH_2(CO)(κ^2-P,P-PNP)(py) complex. In both cases, two atomic map numbers were assigned in the SMILES notation to define the coordination sites, creating a vacant site. The unassigned atomic map number was then set to bind the pyridine ligand.

After generation, a post-generation filtering step was applied using the Universal Force Field (UFF) to retain only relevant conformers. These conformers were exported as XYZ files, containing full atomic coordinates suitable for downstream quantum-chemical calculations or further computational screening. This process, shown in step 2 of Figure 3.3, resulted in 24 unique structures, varying in pincer backbone (NNN, PNP, NONON, or PONOP) and substituents. Additionally, 18 substrate-specific structures were generated, featuring either the replacement of the carbonyl ligand or the displacement of one pincer donor atom by pyridine, with further variation in substituents.

Initial screening of conformational space

To identify the lowest-energy stereoisomer and conformer configuration for further calculations, MACE was employed to initially screen the conformational space of the RuH_2(CO)(κ^3-PNP) reference complex against its structurally related analogues RuH_2(CO)(κ^3-$NNNR_2$), RuH_2(CO)(κ^3-PONOP), and RuH_2(CO)(κ^3-NONON). A custom Python script assessed the energetic preferences of ligand configurations across various isomers and substituents by processing MACE-generated XYZ files. This script reads multiple conformers from each file and extracts their associated energies in kcal/mol. All conformer energies are computed using the Universal Force Field (UFF) [19].

The global minimum energy conformer was identified as:

$$E_{\text{best}} = \min_{i,j} E_{i,j}, \tag{3.2}$$

where $E_{i,j}$ represents the energy of conformer j in isomer i.

The relative energies of all other conformers were computed as:

$$\Delta E_{i,j} = E_{i,j} - E_{\text{best}}. \tag{3.3}$$

Conformers were ranked by relative stability. Additionally, the mean and standard deviation of relative energies across all conformers were computed:

$$\mu = \frac{1}{N} \sum_{i,j} \Delta E_{i,j}, \tag{3.4}$$

$$\sigma = \sqrt{\frac{1}{N} \sum_{i,j} \left(\Delta E_{i,j} - \mu\right)^2}, \tag{3.5}$$

where N is the total number of conformers [29, 30].

To visualise the energy distribution, the script produced histograms with kernel density estimates:

$$\widehat{f}(x) = \frac{1}{nh} \sum_{i=1}^{n} K\left(\frac{x - x_i}{h}\right), \tag{3.6}$$

where $\widehat{f}(x)$ is the estimated probability density, K is the kernel function, h is the bandwidth, and x_i are the data points. Scatter plots colour-coded by isomer facilitated comparative analysis [31].

3.2.3 Density functional theory calculations

The geometries generated by MACE were further refined through geometry optimisation and frequency calculations using the quantum-mechanical method of Density Functional Theory (DFT). These computations were performed using the ORCA 6.0.1 software package on the national supercomputer Snellius [25, 32]. To streamline the workflow, all MACE-generated XYZ output files were automatically converted into ORCA input files (.inp) using a custom Python script executed within the PyMOL interface [33]. The calculations employed the PBE0 hybrid functional [34] combined with Grimme's D3BJ dispersion correction with Becke–Johnson damping (D3BJ) [35, 36], along with the def2-SVP basis set and the auxiliary def2/J basis set to enhance computational efficiency [37, 38].

All calculations were performed within an unrestricted Kohn–Sham (UKS) framework for a singlet spin multiplicity (multiplicity = 1). The geometry optimisation involved repeatedly calculating the total energy and its gradients on the atoms, then adjusting their positions with a trust-region Newton–Raphson method until the energy and forces were sufficiently small, indicating a stable structure on the potential energy surface. Following geometry optimisation, vibrational frequency calculations were conducted to verify the nature of the stationary points. These calculations involve determining the second derivatives of the energy with respect to atomic positions, either through direct analytical methods or numerical differentiation by small atomic displacements. The vibrational frequencies help confirm whether the optimised structure corresponds to a true minimum or a transition state.

Additionally, the vibrational data provided essential thermodynamic corrections, including zero-point energy and finite-temperature contributions, enabling accurate calculations of free energy and enthalpy. All calculations were performed at 298.15 K and 1 atm, utilising 24 parallel processors with 1500 MB of core memory per process.

3.2.4 Gibbs free energy calculations

Exploration of ligand fluxionality

To extend the MACE-based initial conformational screening, ligand fluxionality in the $RuH_2(CO)(\kappa^3$-PNP) reference complex was probed for two different isomers. This was done by comparing the conformational energetics of the reference complexes with those of structurally analogous complexes featuring $NN_{py}N$, $NON_{py}ON$, and $PON_{py}OP$ backbones.

To assess ligand fluxionality through conformational energetics, the relative Gibbs free energy ($\Delta\Delta G$) between distinct isomeric states was calculated. A Python script extracted Gibbs free energies from ORCA output files. For each ensemble of 50 conformers sharing the same backbone and substituent R-group, the single conformer with the lowest Gibbs free energy was identified. This conformer represented the most thermodynamically stable configuration under standard conditions and was selected as the reference. The difference in Gibbs free energy between the two most stable conformers, one from each isomer, was then calculated as:

$$\Delta\Delta G = G_{\text{isomer A, best}} - G_{\text{isomer B, best}}. \tag{3.7}$$

Here, a positive value indicates that isomer B is more stable (i.e., $G_{\text{B, best}} < G_{\text{A, best}}$), while a negative value favours isomer A. This $\Delta\Delta G$ serves as an indicator of fluxional behaviour: if the barrier separating the two isomers is low, interconversion between them becomes feasible at room temperature, indicating significant ligand fluxionality.

Finally, the globally preferred isomer, the one with the lowest Gibbs free energy within each ligand family, was chosen as the reference structure for subsequent hemilability calculations.

Quantifying hemilability through pyridine binding energy

For each pathway illustrated in Figure 3.2 (Section 3.1), the pyridine binding energy is computed as a quantitative descriptor to assess the catalytic performance of these substitutions. Gibbs free energies were extracted from the DFT-optimised substrate-specific structures of each pathway. These energies were used to calculate the total energy change under standard conditions upon addition of the pyridine substrate relative to the most stable configuration of the initial complex within each ligand family (using a 50-conformer ensemble).

Based on Equation (3.1), the following specific equations for the pyridine binding energy are derived for each pathway:

Substitution of the carbonyl auxiliary ligand by pyridine, ΔG_1:

$$\Delta G_1 = G_{\mathrm{RuH_2(py)(\kappa^3\text{-}PNP)}} - G_{\mathrm{RuH_2(CO)(\kappa^3\text{-}PNP)}} - G_{\mathrm{pyridine}} + G_{\mathrm{CO}}. \tag{3.8}$$

The central donor atom N of the pincer backbone dissociates and pyridine coordinates, ΔG_2:

$$\Delta G_2 = G_{\mathrm{RuH_2(CO)(\kappa^2\text{-}P,P\text{-}PNP)(py)}} - G_{\mathrm{RuH_2(CO)(\kappa^3\text{-}PNP)}} - G_{\mathrm{pyridine}}. \tag{3.9}$$

The side-arm PR_2 of the pincer backbone dissociates and pyridine coordinates, ΔG_3:

$$\Delta G_3 = G_{\mathrm{RuH_2(CO)(\kappa^2\text{-}P,N\text{-}PNP)(py)}} - G_{\mathrm{RuH_2(CO)(\kappa^3\text{-}PNP)}} - G_{\mathrm{pyridine}}. \tag{3.10}$$

The free energy differences (Equations 3.8–3.10), representing the binding free energy of pyridine, quantify the thermodynamic favourability of ligand substitution by pyridine as the incoming substrate. A more negative ΔG indicates a stronger driving force for pyridine to either displace (i) the auxiliary carbonyl ligand to form $RuH_2(py)(\kappa^3\text{-PNP})$, (ii) the phosphorus donor side arm to generate $RuH_2(CO)(\kappa^2\text{-P,N-PNP})(py)$, or (iii) the central nitrogen atom of the pincer backbone to yield $RuH_2(CO)(\kappa^2\text{-P,P-PNP})(py)$. This thermodynamic preference highlights the most energetically favourable coordination pathway and thereby determines the overall hemilability character of the complex.

3.2.5 Descriptor calculations

The next step involved calculating steric and geometric descriptors in relation to pyridine binding energy. The P–M–P bite angle reflects electronic and geometric constraints from the pincer backbone. Larger P–M–P values (more open angles) may facilitate pyridine access to the metal centre, lowering the Gibbs free energy of binding [39]. Conversely, smaller or more constrained angles hinder ligand approach, raising the Gibbs free energy of binding [40]. The buried volume reflects steric constraints: higher values indicate greater steric bulk, which can impede pyridine coordination, leading to less favourable binding energies; lower buried volumes favour binding by providing more accessible space [41, 42].

To calculate the bite angle (section 2.1.2) of the DFT-optimised complexes, a custom Python script was used. This script constructs vectors from the ruthenium centre to each phosphorus atom, using Cartesian coordinates extracted from the ORCA output files.

Two vectors ($\vec{v}_1$ and $\vec{v}_2$) are created by connecting the ruthenium atom to each phosphorus atom in the pair:

$$\vec{v}_1 = \vec{r}_{p1} - \vec{r}_{\mathrm{ru}}, \quad \vec{v}_2 = \vec{r}_{p2} - \vec{r}_{\mathrm{ru}}, \tag{3.11}$$

where $\vec{r}_{p1}$, $\vec{r}_{p2}$, and $\vec{r}_{\mathrm{ru}}$ are the position vectors of the two phosphorus atoms and the ruthenium atom, respectively. Each vector is then normalised to unit length:

$$\hat{v}_1 = \frac{\vec{v}_1}{\|\vec{v}_1\|}, \quad \hat{v}_2 = \frac{\vec{v}_2}{\|\vec{v}_2\|}. \tag{3.12}$$

The angle between these normalised vectors is computed using the dot product:

$$\theta = \arccos(\hat{v}_1 \cdot \hat{v}_2). \tag{3.13}$$

The final P–Ru–P bite angle (in degrees) is:

$$\text{P–Ru–P bite angle} = \frac{180^\circ}{\pi} \arccos(\hat{v}_1 \cdot \hat{v}_2). \tag{3.14}$$

The percent buried volume ($\%V_{bur}$) was calculated using the graphical interface of the SEQCROW plugin for UCSF ChimeraX, a cross-platform 3D molecular visualisation program [43]. SEQCROW, an AaronTools-based extension of ChimeraX, enhances its functionality by providing tools for constructing, modifying, and analysing complex molecular structures, including the computation and visualisation of molecular descriptors [23].

$\%V_{bur}$ was determined using the Buried Volume tool in SEQCROW [44]. First, the pincer ligand atoms surrounding the ruthenium catalyst centre were selected. The selection was then changed to the ruthenium atom itself, after which the tool automatically computed the percent buried volume for the specified metal centre. Additionally, the tool can generate a cutout representation of the buried volume, illustrating the regions of space occluded by ligands relative to the metal centre (Figure 3.5).

Van der Waals radii were assigned with a scaling factor of 1.17, and a probe sphere of 3.5 Å radius was centred on the metal atom.

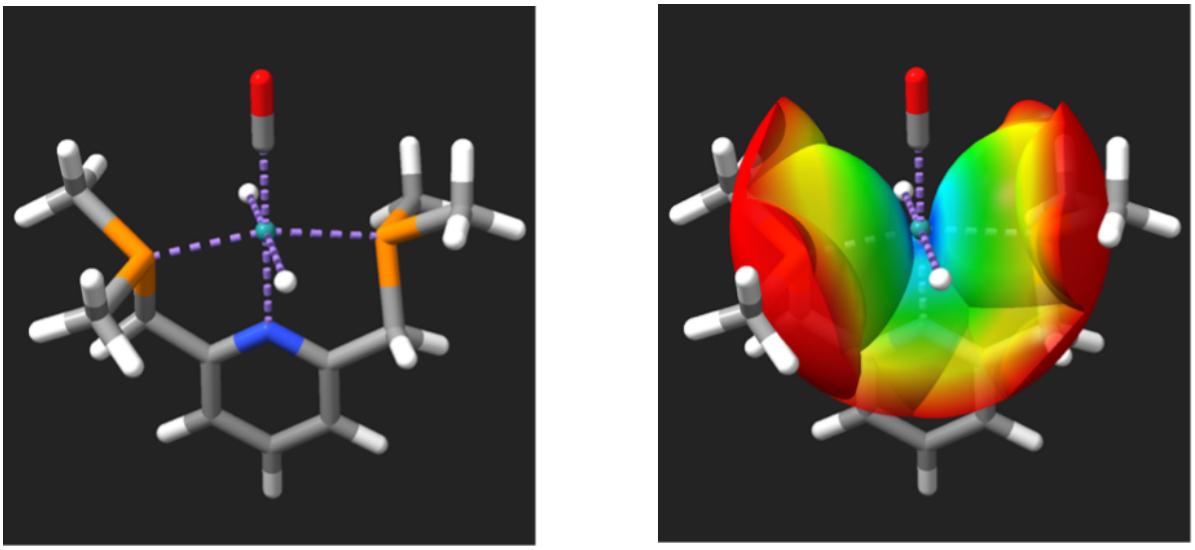

(a) Metal PNP pincer complex

(b) Buried volume cutout (3.5 Å sphere)

Figure 3.5: Visualisation of buried volume calculation using SEQCROW.

.

4

Results and Discussion

4.1 Conformational exploration and ligand fluxionality

Following the initial screening of the conformational space as detailed in Section 3.2.2, we examined whether the observed trends in configurational preferences, particularly the preference for the *cis*-H_2 isomer, persist across varying backbone structures and substituents in pincer ligand complexes. The initial screening revealed comparable stability between both isomers in most cases, indicating inherent configurational flexibility within these systems.

The initial conformer search was conducted in MACE using molecular mechanics (MM) with the Universal Force Field (UFF). Subsequent DFT geometry optimisations and frequency calculations refined the relevant conformers, as detailed in Section 3.2.3. This DFT refinement proved essential, as the trends from the MM conformer search in MACE revealed significant differences from DFT predictions in isomeric preference and the energetic distribution of the systems (see Appendix B.1). While UFF proved to be an effective method for initial screening, the difference with the DFT results highlights the necessity for further optimisation of these pincer complexes using quantum mechanical computations for accurate energetic assessments.

To quantify and further investigate the configurational flexibility observed in the initial screening, the thermodynamic accessibility of each isomer under typical reaction conditions was calculated using Boltzmann statistics (Equation 2.3, Section 2.2). Conformations within a 10 kJ/mol energy window above the global minimum were deemed thermodynamically accessible. This threshold aligns with the principle that catalyst populations follow a Boltzmann distribution under standard homogeneous catalysis conditions, where 5–50% of the catalyst population resides in metastable conformations within this energy range [45].

From the DFT optimizations and frequency calculations of the initial complex, $RuH_2(CO)(\kappa^3\text{-PNP})$, the Gibbs free energy values for the conformer ensemble within each ligand framework were obtained. For each ligand variant, the lowest-energy conformer of each isomer was identified, and the difference in Gibbs free energy ($\Delta\Delta G$) between the most stable conformers of isomer 0 (*trans*-H_2 configuration) and isomer 1 (*cis*-H_2 configuration) was computed according to Equation 3.7 (Section 3.2.4).

The Gibbs free energy differences were calculated across four backbone architectures (PNP, PONOP, NONON, NNN) and six substituents (Bu, Cy, iPr, Me, Ph, tBu), with $\Delta\Delta G$ values ranging from −1.69 to 41.90 kJ/mol, shown in Figure 4.1.

The magnitude of the Gibbs free energy difference ($\Delta\Delta G$) provides a direct measure of ligand fluxionality, revealing the catalyst's tendency to interconvert between isomeric conformations. Two scenarios were considered: (1) systems with small $\Delta\Delta G$ (< 10 kJ/mol) values exhibit high fluxionality, enabling interconversion between isomeric conformations; (2) systems with large $\Delta\Delta G$ values (> 10 kJ/mol) show a strong preference for a particular configuration, yielding well-defined, structurally rigid catalytic species.

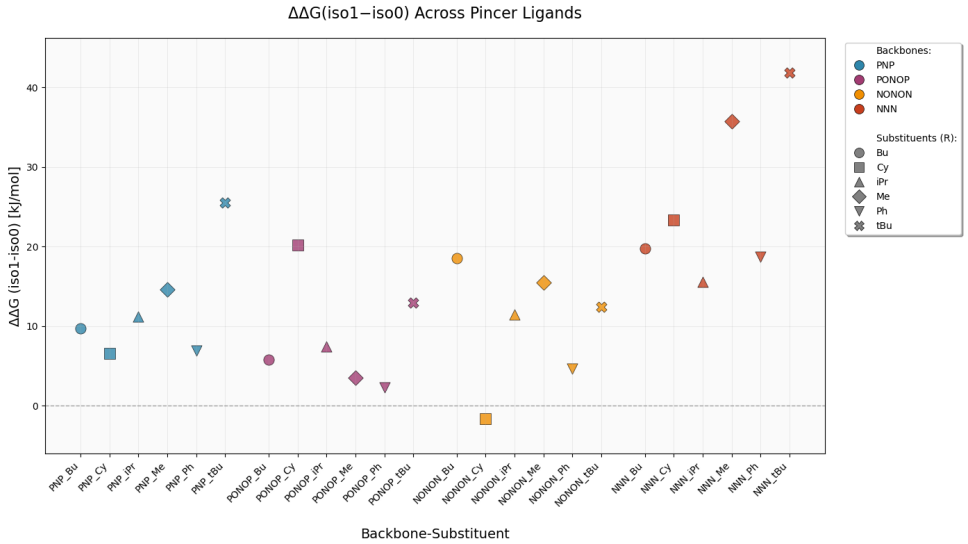

Figure 4.1: Relative Gibbs free energy differences ($\Delta\Delta G$) between two isomers of [$RuH_2(CO)(R_2–X–R_2)$] pincer complexes. $\Delta\Delta G = G(iso_1) - G(iso_0)$ values (in kJ/mol) were calculated from DFT-optimized structures across four backbone types (X = PNP, PONOP, NONON, NNN; shown by colour) and six substituents (R = Bu, Cy, iPr, Me, Ph, *t*Bu; shown by marker shape). The dashed line at $\Delta\Delta G = 0$ indicates equal stability between the two isomers.

The results of Figure 4.1 indicate that the backbone architecture significantly influences isomeric preferences. PONOP- and PNP-based complexes exhibit the lowest $\Delta\Delta G$ values, indicating fluxional behaviour. In contrast, NNN ligands show the highest $\Delta\Delta G$ values, reaching up to 41.89 kJ/mol for the NNN-*t*Bu system, strongly favouring the *trans*-H_2 configuration. This distinction arises from the O_2-linkers, which form a more constrained chelate ring (Ru–P–O–N) with different bond angles, compared to CH_2-linkers that offer greater rotational freedom.

The NONON-Cy system uniquely favours the *cis*-H_2 configuration ($\Delta\Delta G = -1.69$ kJ/mol). This preference arises from backbone flexibility (Figure 4.2b). The cyclohexyl substituents induce a slight twist in the NONON backbone when the carbonyl ligand is equatorial, allowing a more favourable orientation of the Cy groups compared to the axial CO configuration, where no such backbone flexibility exists (Figure 4.2a). This represents a case where the *cis*-H_2 system can energetically compete with the typically favoured *trans*-H_2 arrangement.

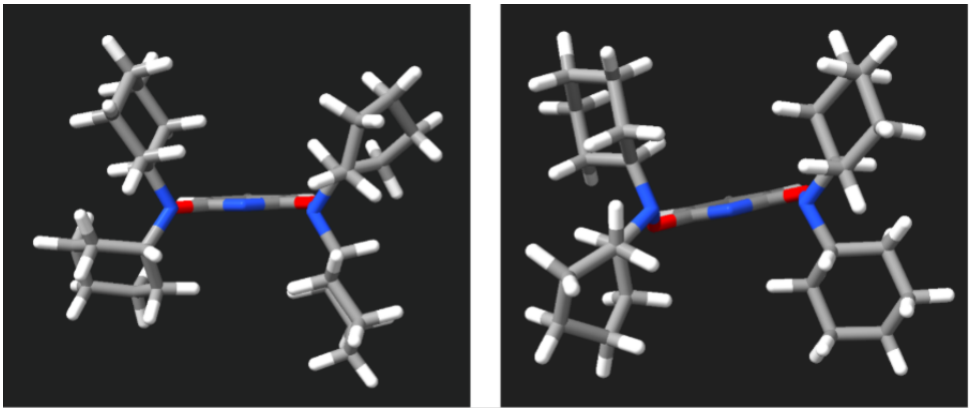

(a) (b)

Figure 4.2: Comparison of NONON-Cy isomers: (a) planar backbone with axial carbonyl (isomer 0), and (b) twisted backbone with equatorial carbonyl (isomer 1).

Tert-butyl groups, being exceptionally bulky, show the strongest geometric preferences among all substituents studied, with $\Delta\Delta G$ values reaching up to 41.90 kJ/mol for NNN backbones. The NNN system exhibits hemilabile behaviour, with both nitrogen arms capable of dissociation, providing substantial conformational freedom. Despite this flexibility, axial CO placement is overwhelmingly preferred.

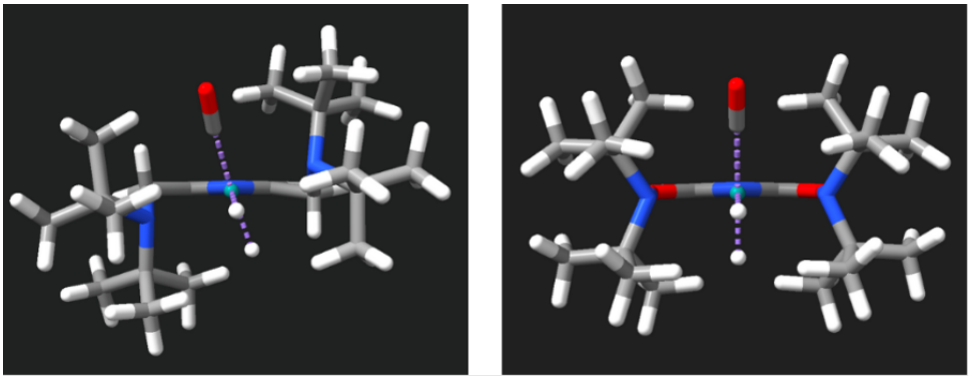

(a) (b)

Figure 4.3: Comparison of *tert*-butyl substituted isomers: (a) NNN system with hemilabile twisted backbone and asymmetric *tert*-butyl positioning, and (b) NONON system with rigid, strained backbone forcing symmetric *tert*-butyl arrangement.

The introduction of rigid O_2-linkers in the backbone reduces $\Delta\Delta G$ from 41.90 to 12.46 kJ/mol, highlighting the significant influence of backbone rigidity on isomeric preferences. These O_2 linkers introduce greater backbone strain, forcing the tert-butyl groups into a symmetric orientation rather than the asymmetric arrangement above and below the backbone plane observed in NNN systems. In the NNN system, the hemilabile nature of the nitrogen side arms induces a twist, offsetting the backbone plane relative to the metal coordination plane (Figure 4.3a). Conversely, the symmetric arrangement imposed by the O_2 linkers in the NONON system allows the equatorial CO ligand to position itself farther from the nitrogen donors. This reduces electronic repulsion and partially compensates for the steric strain (Figure 4.3b).

The same trend is observed for the smallest substituent, methyl, when O_2-linkers are introduced. In the PONOP ligand scaffold, fluxionality is evident ($\Delta\Delta G$ = 3.49 kJ/mol), as the O_2-linkage induces backbone strain. Here, methyl substituents adopt symmetrical arrangements in both isomers, resulting in minimal energy differences between them.

In contrast, the more flexible PNP scaffold exhibits a strong preference for isomer 0 ($\Delta\Delta G$ = 14.60 kJ/mol). This preference arises from a backbone plane twist that accommodates the most favourable conformation (Figure 4.4b). This contrasts sharply with the backbone twist observed in isomer 1, where both pincer arms asymmetrically twist above the aryl pincer plane, imposing a higher energetic penalty to maintain this strained configuration (Figure 4.4a).

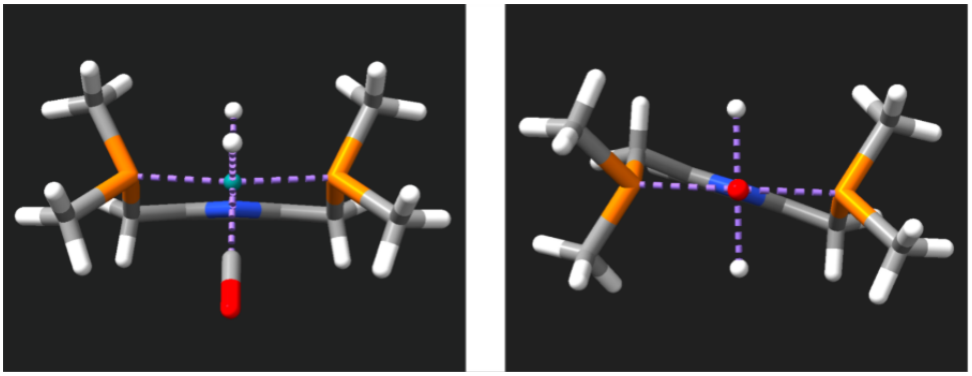

(a) (b)

Figure 4.4: Comparison of methyl-substituted PNP isomers: (a) isomer 1 with asymmetric arm distortion above the aryl plane, and (b) isomer 0 with backbone twist.

For isopropyl, fluxionality is observed between the two isomers only for the PONOP system, in contrast to other backbones, with a $\Delta\Delta G$ of 7.44 kJ/mol. This is due to phosphine ligands with isopropyl substituents adopting a preferential 'umbrella' orientation in the PONOP system, which is less adopted in the other backbones.

Furthermore, phenyl substituents display fluxional behaviour across most backbone types, with the exception of NNN. The planar phenyl groups provide a wider open space in their orientation, minimizing steric hindrance and allowing both isomers to be accommodated in the more flexible PNP backbone as well as in the more rigid NONON and PONOP backbones.

Backbone architecture significantly influences conformational preferences, with O_2-linkers enforcing meridional geometries and restricting flexibility. This rigidity affects $\Delta\Delta G$ by creating symmetric arrangements that reduce steric strain. While bulkier substituents tend to increase $\Delta\Delta G$, backbone flexibility and electronic effects, especially in NNN systems, can override steric factors. Still, *trans*-H_2 configurations are preferred across most systems, making them our reference point for subsequent calculations detailed in the following section.

4.2 Energetic preference of pyridine substitution pathways

To determine the overall hemilable character of the starting complex, $RuH_2(CO)(\kappa^3\text{-PNP})$, the energetic preference of the three substitution pathways (Figure 3.2) towards pyridine coordination is quantified by calculating the binding energies of pyridine for each pathway. These binding energies were derived according to Equations 3.8–3.10 (Section 3.2.4), based on Gibbs free energies obtained from DFT-optimised substrate-specific structures: $RuH_2(py)(\kappa^3\text{-PNP})$, $RuH_2(CO)(\kappa^2\text{-P,P-PNP})(py)$, and $RuH_2(CO)(\kappa^2\text{-P,N-PNP})(py)$ (Figures 3.1b–d). The most thermodynamically stable configuration within each ligand family, identified in Section 4.1, served as the reference state (Table A.2, Appendix A). The results for each pathway are depicted in Figure 4.5 (see Appendix A for full numerical values).

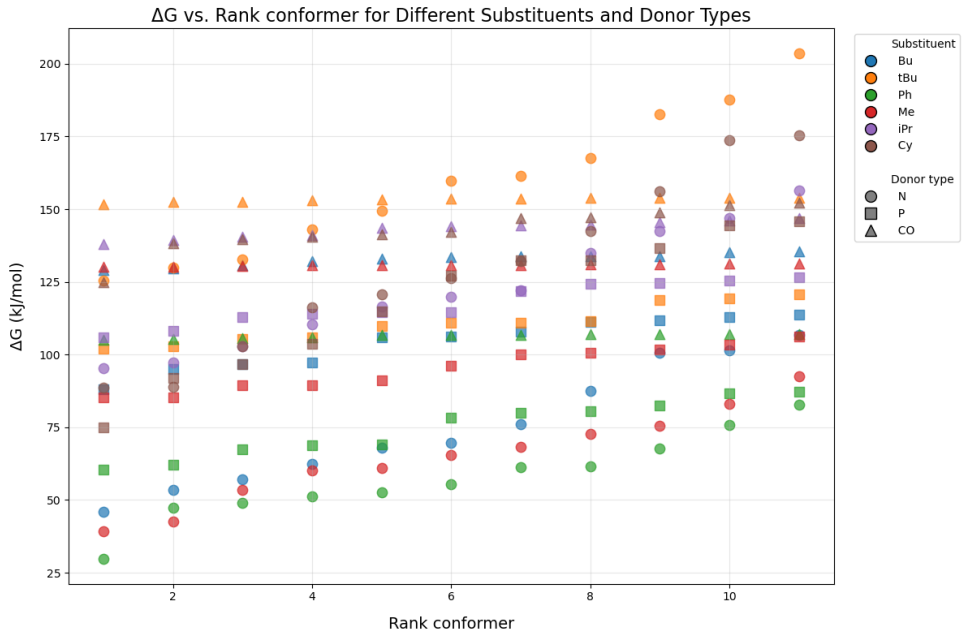

Figure 4.5: Pyridine binding energy (ΔG, in kJ/mol) as a function of conformer rank for RuPNP pincer complexes across three substitution pathways and six substituents. Conformers are ranked in ascending order of binding energy for each substituent–donor combination. Marker shapes indicate the displaced donor type (N, P, CO), and substituents (R = Bu, *t*Bu, Ph, Me, iPr, Cy) are distinguished by colour. For each system, the 11 lowest-energy conformers are displayed to enable consistent comparison across all pathways.

All pathways were thermodynamically unfavorable, as evidenced by their positive pyridine binding energy values. The starting complex, $RuH_2(CO)(\kappa^3\text{-PNP})$, leaves no vacant coordination site available for an additional ligand. When attempting to substitute the carbonyl auxiliary ligand, pyridine binds to a fully coordinated complex, leading to the most unfavorable coordination pathway. This is demonstrated by a mean ΔG of 134.9 kJ/mol (Figure 4.5).

However, the hemilability of either the nitrogen or phosphorus donor atoms in the pincer ligand creates an accessible open site. This allows coordination to the metal center either *cis* to the aryl bond axis (cis ligand void space, Figure 4.6b) or *trans* to the aryl bond axis (trans ligand void space, Figure 4.6a).

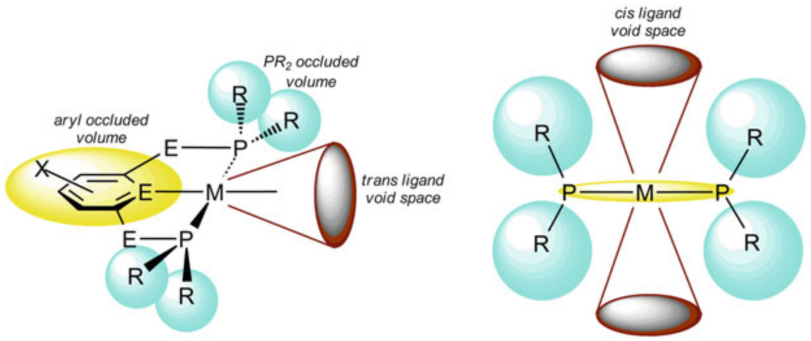

Figure 4.6: Schematic of asymmetric steric influence of lutidine-based PNP pincer ligands: (a) trans ligand void space; (b) cis ligand void space [46].

In this context, these pathways exhibit slightly improved favorability for pyridine coordination. Specifically, dissociation of the phosphorus donor yields a mean ΔG of 103.5 kJ/mol, while dissociation of the nitrogen donor results in a more favorable mean ΔG of 101.4 kJ/mol for pyridine binding. Therefore, the most favorable pyridine coordination pathway overall is the dissociation of the central nitrogen donor atom of the pincer ligand. This pathway demonstrates a large energy span, with most substituents showing ranges from 53 to 88 kJ/mol, and *t*Bu showing the highest range of 78 kJ/mol. The pathway as a whole exhibits an energy span of 173.56 kJ/mol, indicating significant conformational flexibility.

The conformational sensitivity observed in this pathway can be attributed to the structural rearrangements that occur upon binding of pyridine. Notably, the dissociation of the bridging nitrogen donor of the PNpyP pincer creates a vacant coordination site, enabling the pyridine moiety of the lutidine-based pincer ligand to reorient toward the incoming substrate.

This rearrangement promotes π–π stacking between the incoming pyridine substrate and the pyridine ring of the PNpyP pincer. π–π stacking is a noncovalent interaction that occurs between aromatic rings due to attractive forces between their π-electron clouds. When the planar surfaces of aromatic rings are positioned parallel, their delocalized π orbitals overlap, creating a stabilizing interaction that contributes to the overall stability of the structure and reduction of the pyridine binding energy [47].

Consequently, the $RuH_2(CO)(\kappa^2$-P,P-PNP)(py) complex exhibits a strong preference for configurations that favor this ring alignment, with the substituents following the trend (most to least favorable): Ph > Me > Bu > Cy > iPr > *t*Bu.

The phenyl-substituted $RuH_2(CO)(\kappa^2$-P,P-PNP)(py) complex is the most favorable configuration, whereas the *tert*-butyl-substituted analogue is the least favorable. This difference likely stems from π–π stacking interactions and steric effects. In the phenyl-substituted system, π–π stacking between the aromatic rings of the pincer ligand and the coordinated pyridine is strongly favored. The metal center resides slightly above the pincer ligand plane, positioning the pyridine substrate nearly coplanar with the pyridine moiety in the lutidine-derived scaffold. This parallel alignment enhances stabilization through π–π interactions. Consequently, the binding free energy decreases significantly, from 85.38 kJ/mol to 29.89 kJ/mol, indicating a highly favorable interaction (Figure 4.7a and b).

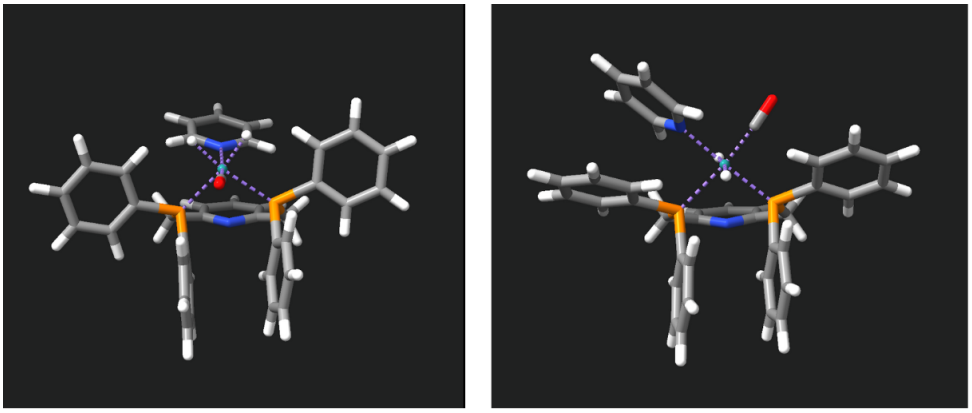

(a) (b)

Figure 4.7: Comparison of phenyl-substituted [$RuH_2(CO)(\kappa^2$-P,P-PNP-Bu)(py)] configurations. (a) Most stable configuration with π–π stacking between pyridine rings (ΔG = 29.89 kJ/mol). (b) Least stable configuration without π–π alignment (ΔG = 85.38 kJ/mol).

In contrast, the *tert*-butyl-substituted system introduces substantial steric hindrance that prevents effective π–π stacking. The bulky *t*Bu groups restrict optimal alignment of the pyridine rings, resulting in the most unfavorable conformation among the series. For comparison, the binding free energy increases from 29.89 kJ/mol for the phenyl-substituted complex to 125.52 kJ/mol for the *tert*-butyl analogue.

Further structural reorganization within the *t*Bu-substituted complex affects its energetics. A more symmetric arrangement of the *tert*-butyl substituents above the meridional plane of the pincer ligand is somewhat more favorable, with a ΔG of 125.52 kJ/mol (Figure 4.8a), compared to 206.46 kJ/mol for the configuration where the substituents occupy asymmetric positions above and below this plane (Figure 4.8b). In the latter case, the bulky groups also block the *cis* ligand void space, leading to further disfavor towards pyridine coordination.

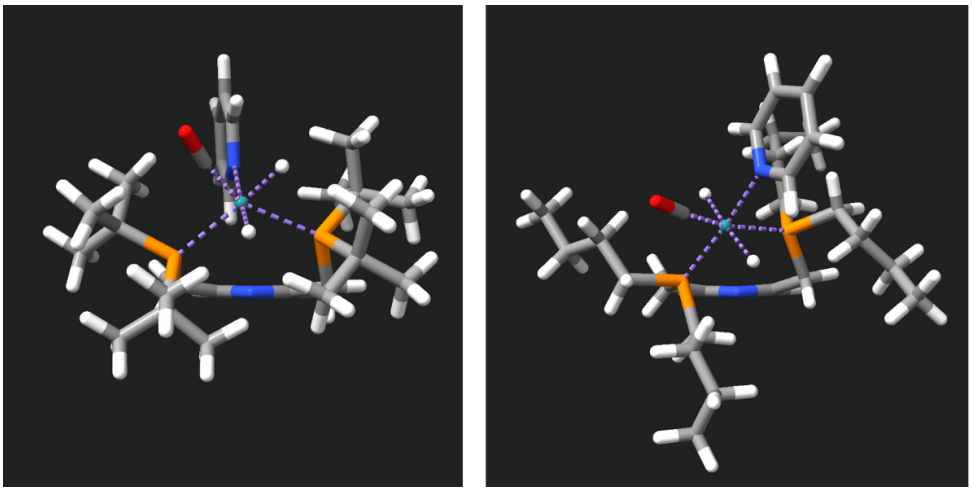

(a) (b)

Figure 4.8: Comparison of *tert*-butyl-substituted $RuH_2(CO)(\kappa^2$-P,P-PNP)(py) configurations. (a) The most stable configuration, with symmetric *t*Bu groups positioned above the meridional plane of the PNpyP pincer ligand (ΔG = 125.52 kJ/mol). (b) The least stable configuration, with asymmetric *t*Bu groups positioned both above and below the meridional plane (ΔG = 206.46 kJ/mol).

For the cyclohexyl-substituted $RuH_2(CO)(\kappa^2$-P,P-PNP)(py) complex, dissociation of the bridgehead nitrogen allows the pyridine substrate to align with the lutidine scaffold, promoting a favorable π–π interaction. In this configuration, the binding free energy is 88.70 kJ/mol (Figure 4.9a).

In contrast, when the cyclohexyl groups are positioned above the plane and π–π stacking is absent, the pyridine binding energy increases to 175.34 kJ/mol, indicating a much less favorable geometry (Figure 4.9b).

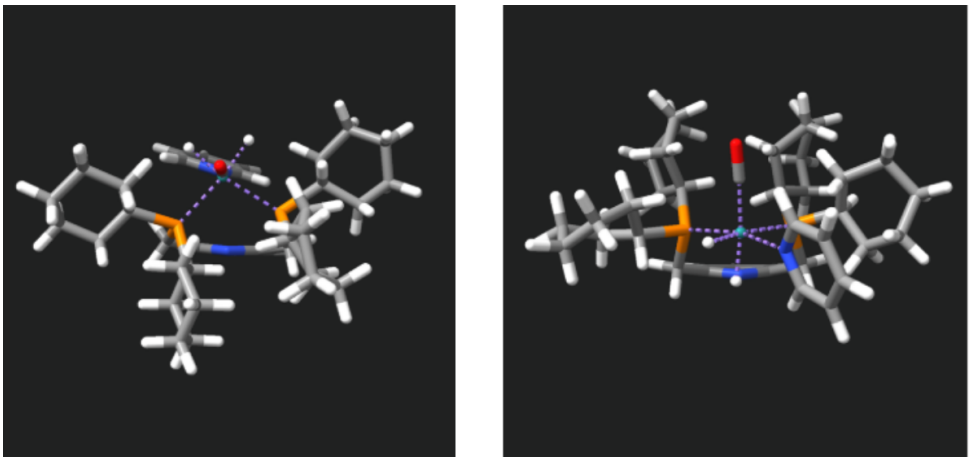

(a) (b)

Figure 4.9: Comparison of cyclohexyl-substituted $RuH_2(CO)(\kappa^2$-P,P-PNP)(py) configurations. (a) Most stable configuration with π–π stacking alignment (ΔG = 88.70 kJ/mol), and (b) least favorable configuration without π–π stacking (ΔG = 175.34 kJ/mol).

The isopropyl and cyclohexyl substituents exhibit a subtle energetic inversion in stability. When the pyridine binding energy for both increases, favoring pyridine coordination, the Cy-substituted configuration is preferred over the *i*Pr system. Conversely, when pyridine coordination becomes less favorable, the *i*Pr-substituted complex gains an energetic advantage over the Cy analogue, with a ΔG difference of 18.96 kJ/mol.

This trend might arise from the fact that the *i*Pr configuration positions the metal center above the meridional pincer plane, leveraging the smaller *i*Pr groups to permit open access to the *cis* coordination site (Figure 4.10a). This arrangement allows the pyridine substrate to approach the metal center more freely from the rear.

In contrast, the Cy-substituted configuration positions the metal center only slightly above the plane. The bulkier Cy substituents sterically block access to the *cis* site, hindering substrate approach. This steric hindrance increases the pyridine binding energy from 156.39 kJ/mol (for the *i*Pr-substituted analogue) to 175.34 kJ/mol (Figure 4.10b).

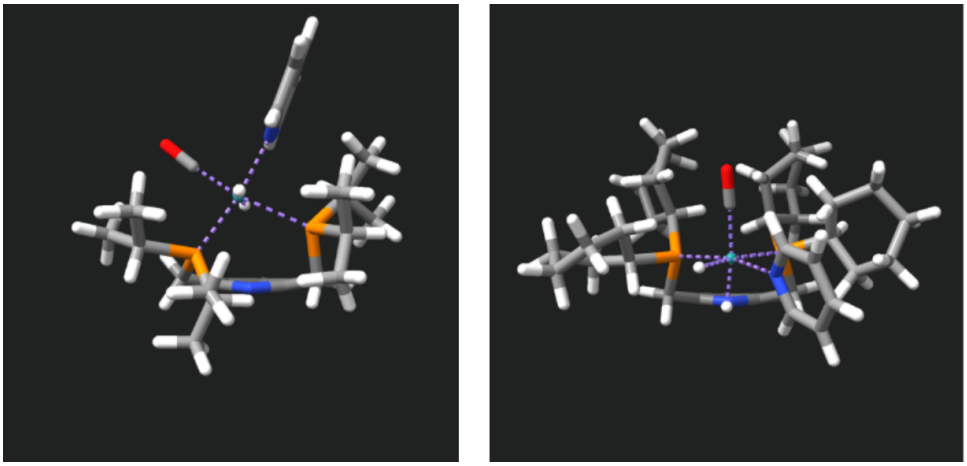

(a) (b)

Figure 4.10: (a) *i*Pr-substituted $RuH_2(CO)(\kappa^2$-P,P-PNP)(py) with access to the *cis* coordination site (ΔG = 156.39 kJ/mol), and (b) Cy-substituted $RuH_2(CO)(\kappa^2$-P,P-PNP)(py) with a sterically blocked *cis* coordination site (ΔG = 175.34 kJ/mol).

In the case of butyl-substituted $RuH_2(CO)(\kappa^2$-P,P-PNP-Bu)(py), the most stable configuration exhibits a pyridine binding energy of 45.86 kJ/mol, whereas the least stable configuration has a binding energy of 123.26 kJ/mol.

This difference in the binding energy of pyridine arises from the open site formed in the most favourable configuration, where alignment of the pyridine substrate with the lutidine-derived pyridine ring of the pincer ligand enables π–π stacking (Figure 4.11a). In contrast, when the pyridine is not aligned with the ligand's aromatic ring, the configuration becomes unfavourable (Figure 4.11b).

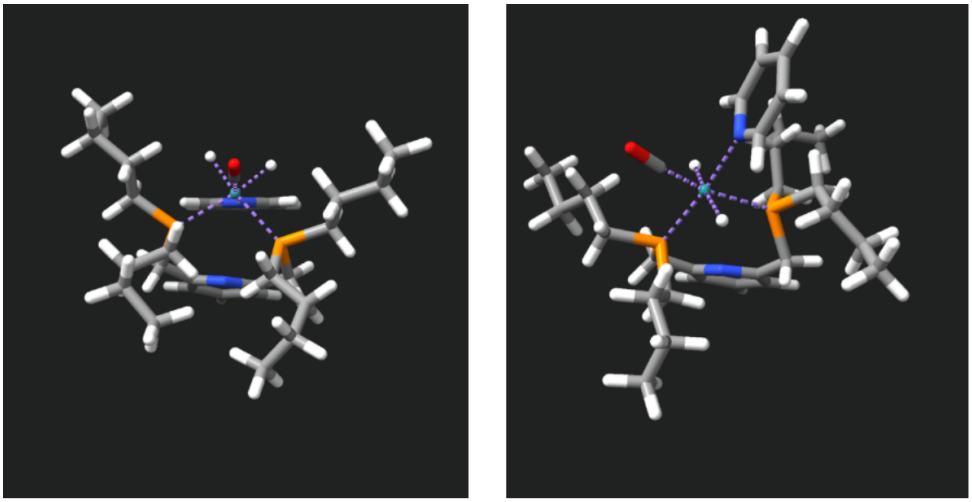

(a) (b)

Figure 4.11: Comparison of butyl-substituted $RuH_2(CO)(\kappa^2$-P,P-PNP-Bu)(py) configurations. (a) Most stable configuration with π–π stacking between pyridine rings (ΔG = 45.86 kJ/mol). (b) Least stable configuration without π–π alignment (ΔG = 123.26 kJ/mol).

The substitution of the carbonyl ligand by the pyridine substrate to form the $RuH_2(py)(\kappa^3\text{-PNP})$ complex represents the least thermodynamically favorable pyridine coordination pathway. The pyridine binding energy follows a trend with respect to the phosphine substituents, ordered from most to least favorable: Ph < Cy < Bu < Me < *i*Pr < *t*Bu.

Notably, the carbonyl substitution pathway exhibits a narrow energy spread across the 11 lowest-energy conformers, ranging from 1 to 8 kJ/mol in most cases (Figure 4.5). This minimal conformational dependence indicates that different conformational states do not significantly influence pyridine binding in this pathway. This behavior likely arises from the structural rigidity imposed by the meridional coordination geometry, which constrains the flexibility of the pincer ligand and leaves the spatial arrangement of the substituents as the key determinant of pyridine binding energy.

The methyl group shows the smallest conformational variation for pyridine coordination in the $RuH_2(py)(\kappa^3\text{-PNP})$ complex, with an energy range of just 1.01 kJ/mol. Conversely, the cyclohexyl substituent shows the largest variation, with 27.34 kJ/mol, indicating significant conformational flexibility affecting pyridine coordination. This flexibility becomes even more evident in an expanded ensemble of 100 conformers, with pyridine binding energies spanning from 124.92 to 237.85 kJ/mol.

The substantial energetic variation in the cyclohexyl-substituted system may be attributed to specific conformational preferences arising from the non-planar character of the cyclohexyl rings. Unlike phenyl substituents, whose planarity enables greater conformational flexibility, the structure of cyclohexyl groups enforces more rigid coordination geometries.

These bulky substituents create significant steric hindrance around the metal center, resulting in a more confined metal pocket. The pyridine binding energy demonstrates strong dependence on the spatial orientation of the cyclohexyl substituents on the phosphine arms, with PNpyP backbone twisting occurring to accommodate favorable cyclohexyl ring orientations. While this enforced rigidity contributes to complex stabilization, it simultaneously restricts substrate accessibility to the metal center, explaining the wide range of pyridine binding energies observed across the conformational ensemble.

The Ph-substituted $RuH_2(py)(\kappa^3\text{-PNP})$ complex demonstrates the most favorable binding energy at 104.97 kJ/mol, whereas the *t*Bu-substituted derivative shows the least favorable value, with a binding energy of 151.63 kJ/mol. The *t*Bu substituent, despite being the bulkiest group examined, displays a small conformational variation of only 2.27 kJ/mol, which suggests that its steric demand enforces highly constrained conformations. The large steric bulk of *tert*-butyl groups presumably restricts access to the metal center and enforces a rigid meridional coordination geometry.

In the *tert*-butyl-substituted system, the PNpyP backbone twist induced to accommodate the *t*Bu substituents in the spatial arrangement restricts access to the *cis* ligand void space, rendering this configuration the least favorable for pyridine coordination in the $RuH_2(py)(\kappa^3\text{-PNP})$ complex (Figure 4.12b).

The phenyl substituents provide moderate steric bulk while maintaining greater conformational flexibility than their *tert*-butyl counterparts due to their planar aromatic nature. These groups also induce a twist in the PNpyP backbone. Their flexibility and planar surface allow for optimal orientation, maintaining accessibility to the *cis* void space. Furthermore, the arrangement of the phenyl substituents creates a wider open space for substrate approach to the *trans* ligand void space. The accessibility of both *cis* and *trans* coordination sites makes the phenyl-substituted $RuH_2(py)(\kappa^3\text{-PNP})$ complex the most favorable configuration for pyridine coordination along this substitution pathway (Figure 4.12a).

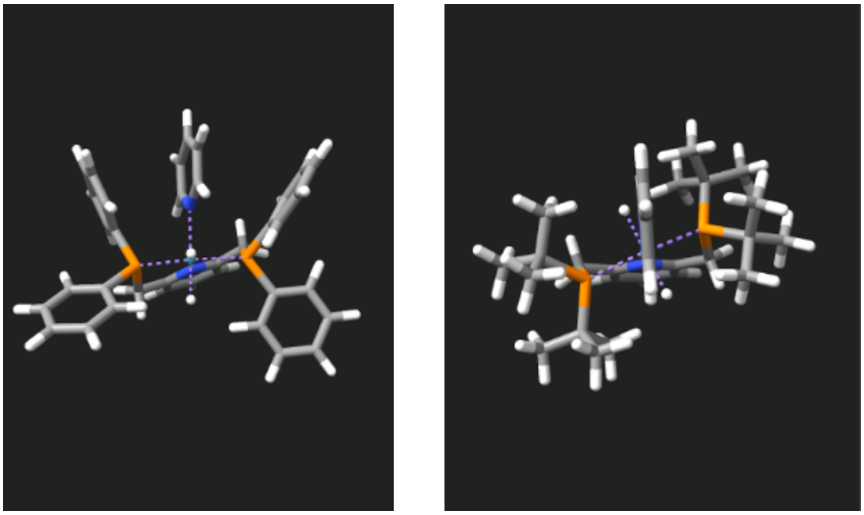

(a) (b)

Figure 4.12: (a) Ph-substituted $RuH_2(py)(\kappa^3\text{-PNP})$ (ΔG = 104.97 kJ/mol); (b) *t*Bu-substituted $RuH_2(py)(\kappa^3\text{-PNP})$ (ΔG = 151.63 kJ/mol).

Interestingly, certain substituent combinations reveal cases where dissociation of the phosphorus donor of the $RuH_2(\kappa^3\text{-PNP})$ pincer backbone becomes more thermodynamically favorable than dissociation of the central nitrogen donor for pyridine coordination, despite the potential for stabilizing π–π interactions in the nitrogen dissociation pathway.

For the *tert*-butyl-substituted complex, dissociation of the central nitrogen donor yields a pyridine binding energy of 125.52 kJ/mol, whereas dissociation of a phosphine arm results in a significantly more favorable binding energy of 102.09 kJ/mol. This 23 kJ/mol preference for the phosphorus dissociation pathway can be rationalized by considering the structural constraints imposed by the pincer architecture and the steric demands of the *tert*-butyl substituents.

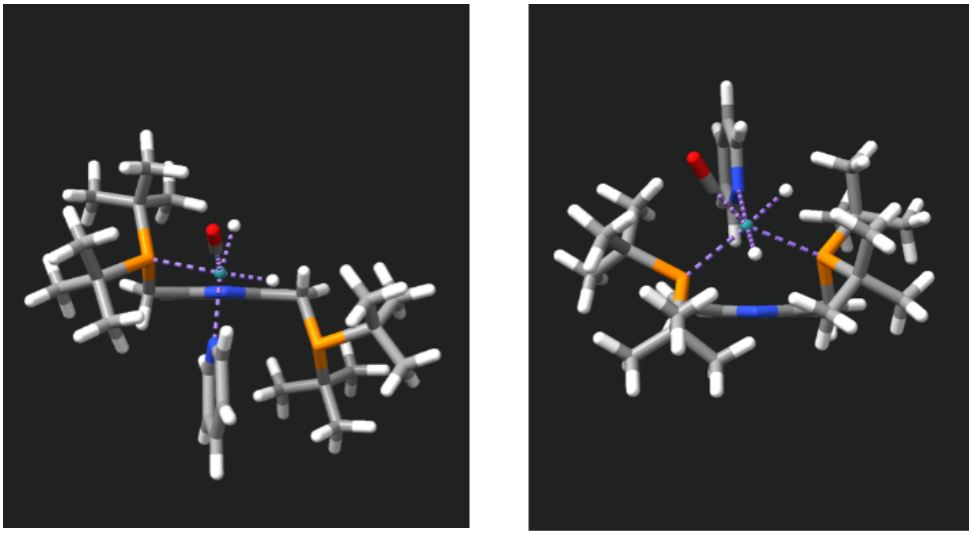

(a) (b)

Figure 4.13: (a) *t*Bu-substituted $RuH_2(CO)(\kappa^2\text{-P,N-PNP})(py)$ (ΔG = 104.97 kJ/mol), and (b) *t*Bu-substituted $RuH_2(CO)(\kappa^2\text{-P,P-PNP})(py)$ (ΔG = 151.63 kJ/mol).

The PNpyP pincer framework enforces a meridional, approximately planar coordination geometry around the ruthenium center, with the two hydride ligands and the carbonyl ligand occupying specific sites in the octahedral coordination sphere, typically in a mutually *cis* arrangement. The dissociation of one phosphine arm generates a vacant coordination site at a peripheral position of the $RuH_2(CO)(\kappa^2$-P,N-PNP)(py) complex, which remains both sterically and electronically accessible for the binding of the incoming pyridine substrate (Figure 4.13a). In contrast, displacing the central nitrogen donor would necessitate significant distortion of the rigid pincer backbone, resulting in a considerable energetic penalty associated with backbone deformation, especially when sterically demanding substituents are present, as they increase strain through restricted conformational flexibility (Figure 4.13b).

A similar pattern emerges for the cyclohexyl-substituted system, where nitrogen donor dissociation yields a pyridine binding energy of 88.70 kJ/mol, while phosphine arm dissociation produces a more favorable value of 74.97 kJ/mol. Even when π–π stacking between the substrate pyridine and the pyridine moiety of the pincer backbone could occur (Figure 4.14b), the steric constraints imposed by bulky, non-planar cyclohexyl substituents appear to favor phosphine arm dissociation.

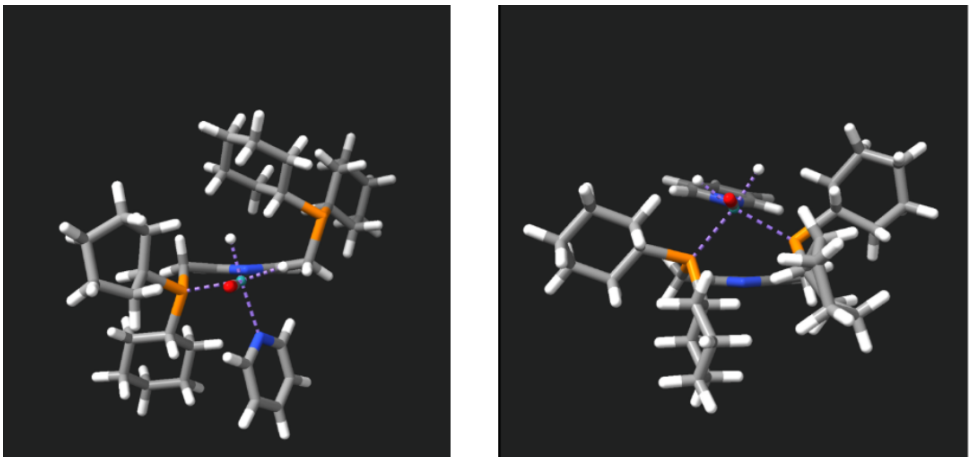

(a) (b)

Figure 4.14: (a) Cy-substituted $RuH_2(CO)(\kappa^2$-P,N-PNP)(py) (ΔG = 74.97 kJ/mol), and (b) Cy-substituted $RuH_2(CO)(\kappa^2$-P,P-PNP)(py) (ΔG = 88.70 kJ/mol).

In these systems, dissociation of the phosphorus donor arm permits conformational flexibility, enabling the bulky substituents to reorient themselves above and below the meridional pincer plane (Figure 4.14a). This conformation provides improved access to the *cis* coordination sites, facilitating substrate approach to the metal center. While π–π stacking can influence binding preferences in systems with small, non-sterically demanding substituents, steric constraints from bulky groups dominate the coordination pathway for pyridine binding, consistently favoring phosphorus over nitrogen dissociation.

The pyridine binding energies for the phosphine dissociation pathway span a range of 85.54 kJ/mol across all substituents. Individually, substituents exhibit narrower ranges from 18 to 27 kJ/mol, except for cyclohexyl, which shows a significantly larger range of 71 kJ/mol. These values span from a minimum of 60.33 kJ/mol in the phenyl-substituted system to a maximum of 145.87 kJ/mol in the cyclohexyl derivative.

This relatively narrow distribution indicates some degree of conformational sensitivity, but with less extreme energy penalties than observed for nitrogen donor dissociation, which exhibits a total range of 173.56 kJ/mol. The pyridine binding free energies for the phosphorus donor side arm dissociation follow the trend Ph < Cy < Me < Bu < *t*Bu < *i*Pr, ordered from most to least favorable.

The phenyl-substituted $RuH_2(CO)(\kappa^2$-P,N-PNP)(py) complex exhibits the most favorable binding energy at 60.33 kJ/mol. In contrast, the isopropyl-substituted system displays the least favorable energetics at 105.98 kJ/mol, representing an increase of 45.7 kJ/mol above the phenyl benchmark. Notably, *i*Pr shows the most dramatic conformational sensitivity, with binding energies ranging from 105.98 to 126.65 kJ/mol across the conformer ensemble.

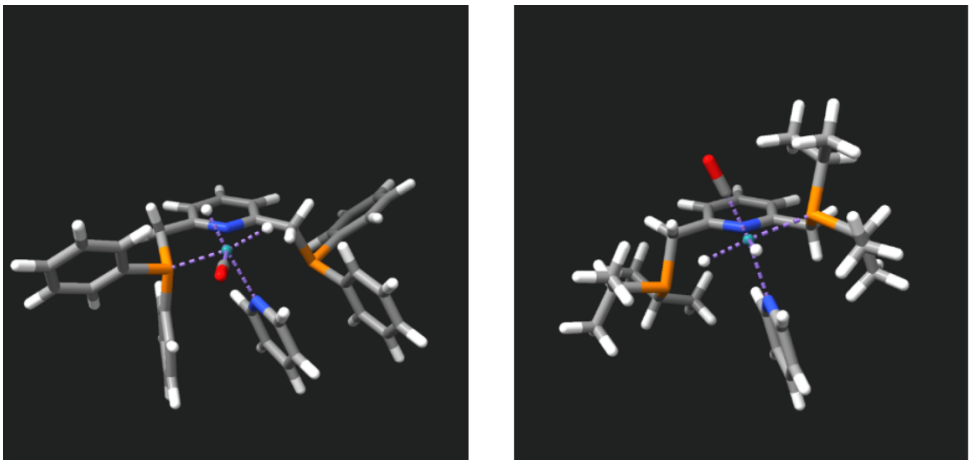

(a) (b)

Figure 4.15: (a) Ph-substituted $RuH_2(CO)(\kappa^2$-P,N-PNP)(py) (ΔG = 60.33 kJ/mol), and (b) *i*Pr-substituted $RuH_2(CO)(\kappa^2$-P,N-PNP)(py) (ΔG = 105.98 kJ/mol).

The planar geometry of phenyl groups provides moderate steric bulk that is considerably less demanding than branched alkyl groups like isopropyl. This planar character in spatial arrangement creates a wider open space and minimizes steric interference with the incoming substrate. In addition, the phenyl groups arrange themselves below or in the same plane as the PNpyP pincer plane upon phosphine dissociation, thereby granting greater access to the *cis* void space where pyridine can bind (Figure 4.15a).

In contrast, the branched isopropyl substituents reorient to positions both above and below the pincer plane, thereby minimizing steric repulsion among the bulky groups (Figure 4.15b). However, this spatial arrangement introduces additional steric bulk and enhances σ-donation to the phosphine arms. The combined steric hindrance and increased electron density at the Ru–P bond destabilises the dissociated state, thus favoring the bound form. These steric and electronic effects collectively disfavor phosphorus dissociation and hinder substrate access to the metal center.

Ultimately, both nitrogen and phosphine dissociation pathways exhibit substantially lower binding energies than carbonyl substitution, demonstrating that substrate binding becomes accessible only when one of the pincer donors dissociates to create a vacant coordination site.

The hemilabile character of the $RuH_2(CO)(\kappa^3$-PNP) pincer complex thus enables substrate binding pathways that would be unattainable in more rigid, fully chelated systems. Among the hemilabile pathways, nitrogen donor dissociation emerges as the thermodynamically most favorable coordination mechanism overall, particularly when combined with phenyl substituents on the phosphine arms and stabilizing π–π stacking interactions.

When the central nitrogen donor detaches from the metal center while the phosphorus donors remain bound, the PNpyP pincer backbone undergoes a structural transformation into a U-shaped cleft. This reorganization creates a spatially confined and chemically tailored binding pocket positioned directly adjacent to the metal center. Simultaneously, the substituents on the phosphine arms effectively shield the flanking coordination sites. This shielding blocks alternative substrate approach pathways while creating an open *trans* ligand void space. As a result, this pocket functions as a guide for the incoming pyridine substrate towards the ruthenium metal center.

4.3 ΔG_{bind} vs buried volume

As discussed in Section 4.2, the *cis* and *trans* ligand void space and the steric influence of the substituents on the phosphine ligands contribute to the asymmetric steric influence of lutidine-based PNpyP pincers. Building on this, we employ the $\%V_{Bur}$ parameter to quantify the overall steric influence on the pincer complexes.

The $\%V_{Bur}$ parameter, as described in Section 2.1.1, is determined by utilizing the SEQROW plugin within UCSF ChimeraX, as detailed in Section 3.2.5. The results for the $\%V_{Bur}$ values of the selected DFT-optimized substrate-specific pincer systems $RuH_2(py)(\kappa^3\text{-RPNP})$, $RuH_2(CO)(\kappa^2\text{-P,P-RPNP})(py)$, and $RuH_2(CO)(\kappa^2\text{-P,N-RPNP})(py)$, with various substituents (R = Me, iPr, tBu, Bu, Ph, Cy), are presented in Figure 4.16 (see Appendix B.2 for individual scatter plots of pyridine binding free energy versus $\%V_{bur}$ for each coordination mode).

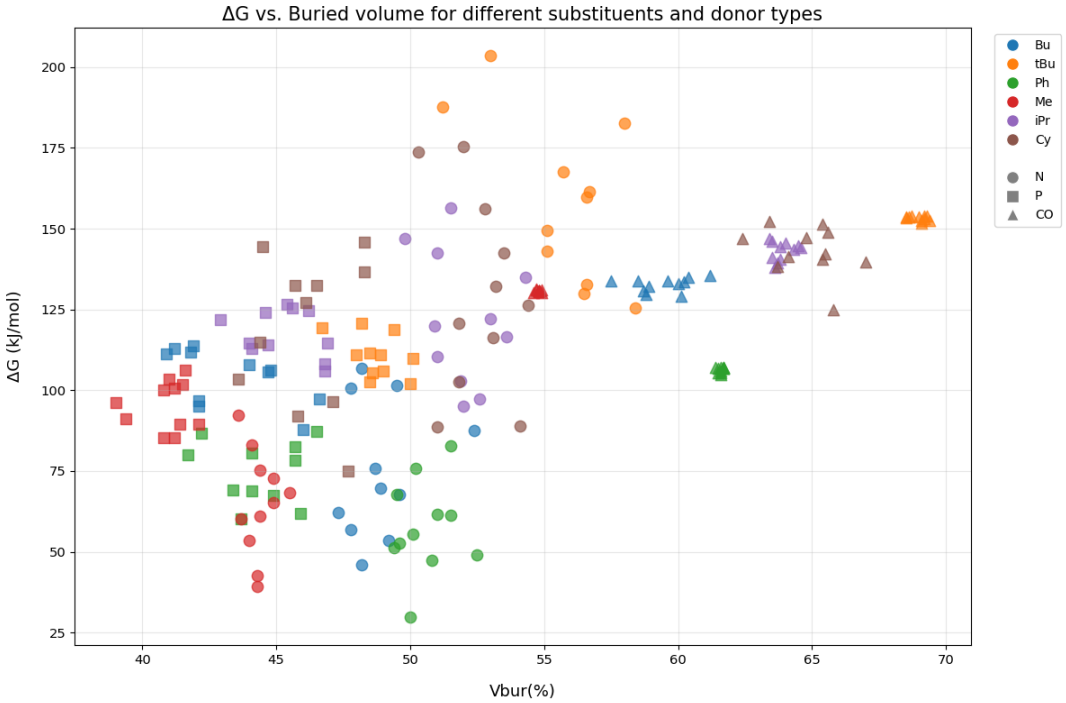

Figure 4.16: Binding free energy of pyridine (ΔG, in kJ/mol) as a function of percentage buried volume (V_{bur}, %) for RuPNP pincer complexes across three substitution pathways and six substituents. Marker shapes indicate the displaced donor type (N, P, or CO), and substituents (R = Bu, *t*Bu, Ph, Me, iPr, Cy) are distinguished by color.

An examination of the $\%V_{bur}$ values in Figure 4.16 shows that the $RuH_2(CO)(\kappa^2\text{-P,P-PNP})(py)$ pincer complex exhibits $\%V_{bur}$ values spanning a range from 43.6% to 58.4%, which corresponds to the largest energy dispersion observed, with ΔG values ranging from approximately 30 to 203 kJ/mol.

For this pincer system, the methyl substituent exhibits the lowest $\%V_{bur}$ values (43.6–45.5%) and the most favorable pyridine binding energy ($\Delta G \approx 39$ kJ/mol). Its compact size minimizes steric clashes while maintaining optimal binding geometry, thereby maximizing substrate accessibility, while *t*Bu has the highest $\%V_{bur}$ (77.4–82.8%) and the most severe energetic penalties (125–203 kJ/mol).

A critical threshold is observed at approximately 50% V_{bur}, beyond which steric destabilization becomes the dominant factor (Figure 4.16). Substituents with lower steric demands (Me, Ph, Bu) below this threshold demonstrate improved binding energetics, whereas bulkier groups (including iPr, Cy, *t*Bu) exceed this threshold, resulting in increased pyridine coordination energies. Notably, the phenyl substituents exhibit moderate $\%V_{bur}$ (49.4–52.5%) but have the lowest ΔG (~30 kJ/mol), indicating that π-stacking interactions effectively compensate for steric effects.

The $RuH_2(CO)(\kappa^2$-P,N-PNP)(py) pincer system appears to exhibit a weaker correlation between the percent buried volume and the pyridine binding energy, displaying a $\%V_{bur}$ range of 11.1% (39.0 to 50.1%). Within this interval, the pyridine binding energies vary considerably, with ΔG values spanning approximately 60 to 146 kJ/mol. The weak correlation between $\%V_{bur}$ and ΔG is visualised as a plateau effect (Figure Xa), where, within the 39–48% V_{bur} range, incremental increases in steric bulk do not consistently correspond to proportional increases in ΔG.

For example, all Cy-substituted $RuH_2(CO)(\kappa^2$-P,N-PNP)(py) conformers span only 4.7% V_{bur} (43.6–48.3%), yet their binding energies vary by 70.9 kJ/mol (75.0–145.9 kJ/mol). This indicates that conformational geometry dominates over absolute steric bulk, as evidenced by the cyclohexyl conformer that most preferentially adopts 47.7% V_{bur} (ΔG = 75.0 kJ/mol) across all pathways. This reflects both the intrinsic conformational preferences of the cyclohexyl substituent and the additional flexibility afforded through phosphine side-arm dissociation.

The pyridine-coordinated $RuH_2(py)(\kappa^3$-PNP) complex displays a $\%V_{bur}$ span of 14.8% across substituents (54.6–69.4%), identical to the span observed for the hemilabile nitrogen-dissociation complex. However, this coordination mode distinguishes itself by exhibiting the highest absolute $\%V_{bur}$ values (54.6–69.4%), which follow a clear substituent hierarchy:

$$\text{Me} < \text{Bu} < \text{Ph} < \text{iPr} \approx \text{Cy} < t\text{Bu}.$$

The trend reflects increasing steric bulk and corresponds to substantial variations in ΔG across substituents, demonstrating this pincer system's inherent sensitivity to steric congestion. This heightened sensitivity likely arises from the fully coordinated nature of the complex, where rigid κ^3-coordination restricts conformational freedom.

For each substituent series, the $RuH_2(py)(\kappa^3$-PNP) system reveals relatively tight energetic clustering (Figure 4.16), consistent with limited conformational flexibility. For instance, the *t*Bu-substituted $RuH_2(py)(\kappa^3$-PNP) complex shows the smallest $\%V_{bur}$ range (0.9%, spanning 68.5–69.4%) of any donor–substituent combination, with a correspondingly narrow ΔG range of 151.6–153.9 kJ/mol. This highlights the rigid character of this coordination mode, which restricts accessible conformations, particularly for sterically demanding substituents.

Across all substituent–donor combinations, methyl consistently exhibits the smallest $\%V_{bur}$ values, regardless of donor type. In contrast, *t*Bu demonstrates the highest steric congestion, especially in the $RuH_2(py)(\kappa^3$-PNP) pincer complex, where $\%V_{bur}$ reaches 68.5–69.4%, compared to the more accommodating $RuH_2(CO)(\kappa^2$-P,N-PNP)(py) hemilabile system, which tolerates *t*Bu with $\%V_{bur}$ values of 46.7–50.1%.

Among the alkyl substituents, cyclohexyl exhibits the widest $\%V_{bur}$ range of 23.4% (43.6–67.0%) across all coordination pathways, reflecting its ability to adopt multiple conformations that minimise steric conflicts. However, this conformational diversity results in pronounced energetic consequences depending on the coordination environment.

In the rigid $RuH_2(py)(\kappa^3$-PNP) pincer system, cyclohexyl displays $\%V_{bur}$ values of 62.4–67.0%, correlating with high energy penalties (124.9–152.3 kJ/mol). Conversely, the energetic profile of cyclohexyl improves dramatically when conformational flexibility is available. Hemilabile phosphine-arm dissociation provides greater steric accommodation (43.6–48.3% V_{bur}, 75.0–145.9 kJ/mol), with the optimal conformer achieving 47.7% V_{bur} and ΔG = 75.0 kJ/mol.

In contrast, nitrogen-donor dissociation exhibits poorer steric tolerance (50.3–54.4% V_{bur}, 88.7–175.3 kJ/-mol), with all conformers exceeding the critical 50% V_{bur} threshold, leading to consistently less favourable binding energetics.

Overall, bulky alkyl substituents (*i*Pr, Cy, *t*Bu) become consistently more unfavourable across all donor types when $\%V_{bur}$ exceeds approximately 50%. This value represents a critical threshold for steric tolerance across the pathways studied.

4.4 ΔG_{bind} vs bite angle

To further understand how the enveloping steric environment of DFT-optimized RuPNpyP pincer complexes influences substrate accessibility, the PRuP bite angle was examined. This PRuP bite angle is defined in Section 2.1.2 and computed using the script outlined in Section 3.2.5. It is primarily determined by the structural constraints of the PNpyP pincer framework and the steric repulsion between substituents on the phosphorus donor atoms. Figure 4.17 presents the PRuP bite angles for all pyridine-coordinated PNpyP complexes examined in this study (see Appendix B.2 for individual scatter plots of pyridine binding free energy versus P-Ru-P bite angle for each coordination mode).

Figure 4.17: Binding free energy of pyridine (ΔG, in kJ/mol) as a function of PRuP bite angle (°) for RuPNP pincer complexes across three substitution pathways and six substituents. Marker shapes indicate the displaced donor type (N, P, or CO), and substituents (R = Bu, *t*Bu, Ph, Me, iPr, Cy) are distinguished by color.

Analysis of the PRuP bite angles in the $RuH_2(CO)(\kappa^2$-P,P-PNP)(py) pincer complex shows that angles below 110° lead to more favorable pyridine coordination. Substituents that adopt angles within the optimal range of 96–102°, namely methyl, phenyl, and butyl, exhibit the lowest pyridine binding energies, ranging from 30 to 107 kJ/mol.

The phenyl substituent merits particular attention, as it demonstrates the most favorable binding energetics (29.89–82.86 kJ/mol) within this pincer system despite approaching the angular threshold (97.7–112.6°), suggesting that stabilizing π–π stacking interactions with the coordinated pyridine substrate provide compensatory effects.

In contrast, the *tert*-butyl substituent uniformly exceeds this critical angle (107.3–116.8°), correlating directly with more unfavorable pyridine binding energetics (ΔG = 126–203 kJ/mol). This correlates with increased steric congestion around the metal center, as indicated by the V_{bur} exceeding 52%, suggesting that steric clashes are likely responsible for the reduced coordination efficiency for the pyridine substrate.

A notable outlier is observed for the cyclohexyl-substituted system, which adopts a bite angle of 120.6°. This wider bite angle correlates with an increase in pyridine binding energy of 27.5 kJ/mol (from 88.7 to 116.2 kJ/mol) relative to the most favorable Cy-substituted configuration (PRuP = 101.6°). This

destabilization arises from the loss of favorable π–π stacking interactions between the coordinated pyridine substrate and the lutidine-derived pyridine ring of the pincer ligand (Figure 4.18a and b).

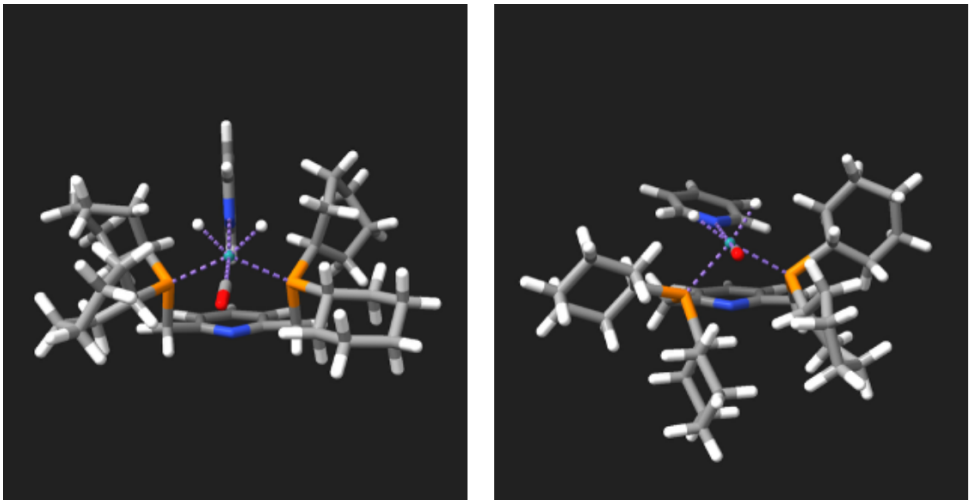

(a) (b)

Figure 4.18: (a) Ph-substituted $RuH_2(CO)(\kappa^2$-P,N-PNP)(py) (ΔG = 60.33 kJ/mol), and (b) *i*Pr-substituted $RuH_2(CO)(\kappa^2$-P,N-PNP)(py) (ΔG = 105.98 kJ/mol).

The hemilabile phosphine sidearm in the $RuH_2(CO)(\kappa^2$-P,N-PNP)(py) complex exhibits the broadest conformational adaptability, accommodating PRuP bite angles spanning 91–145° with the widest range (25.8–53.9°) among all substituents. The cyclohexyl substituent shows the greatest angular variation of 53.9° across all donor–substituent combinations. The most favorable Cy-substituted configuration adopts a P–Ru–P angle of 129.4°, corresponding to a pyridine binding energy of 75.0 kJ/mol (see Figure **??**a).

This flexibility is also evident for the sterically demanding tert-butyl group, which exhibits an angular range of 27.1° (112.5–139.6°). The expanded angular ranges reflect the inherent conformational adaptability of this hemilabile pincer complex, where phosphine sidearm dissociation enables enhanced flexibility, particularly beneficial for sterically demanding substituents.

The $RuH_2(py)(\kappa^3$-PNP) pincer complex exhibits minimal angular variation (156–167°) with tight clustering around 163°, rendering bite angles largely invariant for this coordination mode. With PRuP bite angle ranges restricted to 0.5–8.3° depending on substituent identity, this narrow window reflects the structural constraints of the complex, which restricts conformational degrees of freedom. The geometry imposed by tridentate chelation significantly reduces flexibility and enforces a fixed meridional structure.

The *t*Bu-substituted $RuH_2(py)(\kappa^3$-PNP) complex exhibits the largest PRuP range (8.3°), with two distinct clusters of conformers: one below 160° (PRuP $\approx$ 156°) and another above 160° (PRuP $\approx$ 164°). These isomers appear to adopt either equatorial (PRuP < 160°) or axial (PRuP > 160°) pyridine coordination geometries (Figure 4.19). Despite this difference, both clusters show nearly identical pyridine binding energies, differing by only 0.57 kJ/mol (153.14–153.71 kJ/mol). The tert-butyl substituents appear to adjust their spatial arrangement to minimize steric clashes, accommodating either pyridine coordination mode with comparable stability (Figure 4.19a and b).

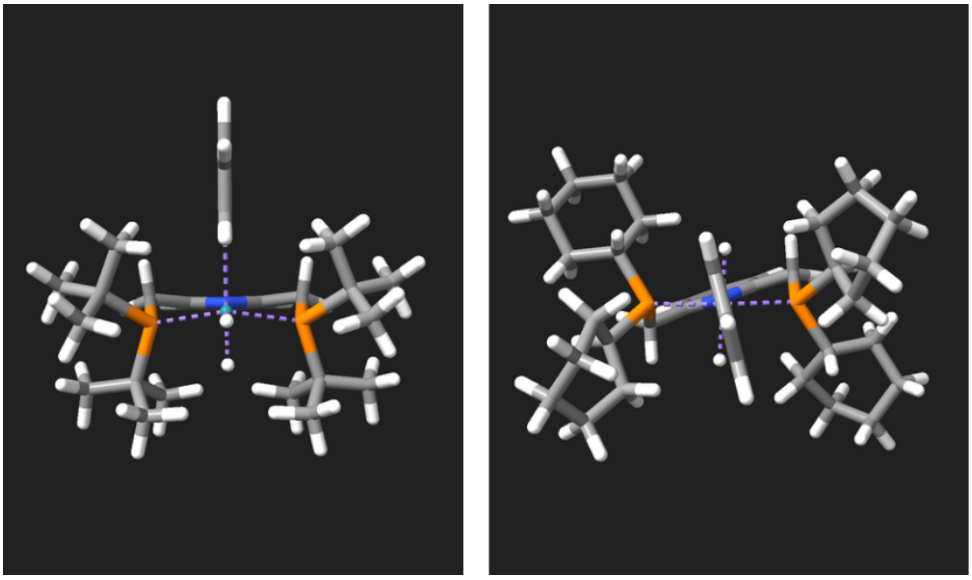

(a) (b)

Figure 4.19: (a) *t*Bu-substituted $RuH_2(py)(\kappa^3\text{-PNP})$ complex with equatorial pyridine (PRuP = 156.3°, ΔG = 153.71 kJ/mol), and (b) *t*Bu-substituted $RuH_2(py)(\kappa^3\text{-PNP})$ complex with axial pyridine (PRuP = 164.6°, ΔG = 153.14 kJ/mol).

Altogether, the data establish universal steric and geometric thresholds for more favorable pyridine coordination across the three coordination pathways examined. The $RuH_2(CO)(\kappa^2\text{-P,P-PNP})(py)$ pincer complex requires $\%V_{bur}$ < 50% and P–Ru–P < 110° for binding energies below 100 kJ/mol. The hemilabile $RuH_2(CO)(\kappa^2\text{-P,N-PNP})(py)$ complex demonstrates substantially more relaxed constraints ($\%V_{bur}$ < 48%, P–Ru–P = 91–145°), accommodating a wider range of substituent profiles through its reversible phosphine dissociation. In contrast, tridentate κ^3-coordination [$RuH_2(py)(\kappa^3\text{-PNP})$] universally imposes the highest pyridine binding energies (ΔG > 100 kJ/mol) across all substituents, despite $\%V_{bur}$ values ranging from 54.6 to 69.4%, demonstrating that rigid geometric constraints (P–Ru–P = 156–167°) and enforced meridional geometry prevent effective steric relief regardless of substituent size.

These findings collectively demonstrate that coordination flexibility, rather than absolute steric minimization, determines substrate accessibility in the Ru–PNP pincer complexes. More favorable substrate binding requires not merely reduced steric bulk, but rather optimized alignment between substituent demands and coordination mode flexibility, with hemilabile systems providing improved performance for sterically demanding substituents through geometric relaxation mechanisms unavailable to rigid coordination architectures.

5

Conclusions and Outlook

This work presents a high-throughput *in silico* screening of ruthenium(II) pincer complexes as potential catalysts for pyridine hydrogenation. The study explores fluxionality in the $RuH_2(CO)(R_2P–N–PR_2)$ (R = Bu, Cy, Me, Ph, *i*Pr, *t*Bu) pincer system, comparing its conformational energetics with those of structurally analogous complexes featuring NNpyN, NONpyON, and PONpyOP backbones. Furthermore, this study systematically investigates the hemilabile behavior of the $RuH_2(CO)(R_2P–N–PR_2)$ pincer complex and the quantitative relationships governing substrate binding through a comprehensive analysis of 48 distinct complex architectures and their substrate-specific derivatives. MACE was employed to generate stereoisomer and conformer libraries across multiple pincer backbones (PNpyP, PONpyOP, NONpyON, NNpyN) without conformational bias, followed by UFF-based pre-screening to identify low-energy candidates. Subsequent geometry optimisations and thermochemical calculations at the PBE0-D3BJ/def2-SVP level of theory in ORCA enabled automated extraction of Gibbs free energies and calculation of pyridine binding energetics across three distinct coordination pathways: central nitrogen donor dissociation, phosphine sidearm dissociation, and auxiliary carbonyl ligand substitution.

The results lead to the general conclusion that the investigated ruthenium(II) pincer complexes are unsuitable for pyridine hydrogenation. This assessment is based on two key findings. First, pyridine binding is thermodynamically prohibitive, as all analyzed conformers across the three pathways exhibited high binding free energies. Second, the conformational landscape revealed that a significant population of conformers outside the global minimum are catalytically irrelevant.

Initial conformational screening and subsequent DFT refinement revealed that $RuH_2(CO)(\kappa^3$-pincer) complexes exhibit considerable configurational flexibility, particularly for systems with flexible pincer backbones such as PNP and PONOP. While the fully coordinated complexes are thermodynamically accessible via Boltzmann distribution under typical homogeneous catalysis conditions, the propensity for interconversion between isomeric states (cis-H_2 and trans-H_2) varies systematically with backbone architecture and substituent properties. Rigid O-linker-containing backbones (NON) enforce strict geometric requirements, strongly favoring trans-H_2 configurations, whereas flexible CH_2-linker systems permit more facile isomerization.

Regarding pyridine binding thermodynamics, the results conclusively demonstrate that substrate coordination becomes accessible exclusively when one of the pincer donor atoms undergoes reversible dissociation through hemilabile behavior. The fully coordinated complex, $RuH_2(CO)(\kappa^3$-PNP), exhibits pyridine binding energies of approximately 135 kJ/mol, making substrate binding highly unfavorable. In sharp contrast, dissociation of either the bridging nitrogen or the phosphine side arm reduces binding energies to the 30–105 kJ/mol range, representing 3–4 fold improvements in thermodynamic favorability. This dramatic differential demonstrates that hemilability is not a passive property but a strategic coordination mechanism enabling substrate access to catalytically competent coordination sites.

The three pyridine coordination pathways examined exhibit distinct energetic profiles, revealing a clear hierarchy of pyridine coordination preferences. Nitrogen donor dissociation emerges as the most favorable pathway overall, with the most optimal binding energies as low as 29.89 kJ/mol for phenyl-substituted systems incorporating π–π stacking stabilization. Phosphorus dissociation represents an intermediate pathway (60–105 kJ/mol) and performs optimally with bulky substituents, as the enhanced conformational flexibility of the phosphine side-arm accommodates steric bulk more effectively. Carbonyl substitution remains largely inaccessible (100–150 kJ/mol).

The analysis also revealed that π–π interactions between incoming pyridine substrates and the pyridine ring of lutidine-derived pincer scaffolds constitute a major stabilizing force in hemilabile complexes, particularly when the bridging nitrogen donor dissociates. The phenyl-substituted system demonstrates this effect most clearly, with binding energies spanning from 29.89 to 85.38 kJ/mol depending solely on whether π–π alignment is achieved. This substantial energetic differential (>55 kJ/mol) highlights the importance of ligand scaffold composition in substrate binding and suggests that design strategies incorporating aromatic central donors directly coupled to catalytic metal centers can exploit aromatic stabilization mechanisms.

A clear ranking of substituent effects emerged from the comprehensive dataset: bulky, non-planar groups (*tert*-butyl, *iso*propyl, cyclohexyl) uniformly disfavor substrate binding more through enhanced steric hindrance and restricted conformational flexibility, while smaller and planar groups (methyl, butyl, phenyl) consistently favor binding more through reduced crowding and maintenance of accessible coordination sites. Notably, the steric effects are not simply additive but demonstrate complex interplay with geometric constraints: in the nitrogen dissociation pathway, *tert*-butyl substitution elevates binding energies by up to 95 kJ/mol relative to phenyl analogues, yet in the phosphorus dissociation pathway, the differential reaches 45 kJ/mol. These differences reflect the distinct accessibility profiles of the two pathways, indicating that steric consequences are geometry-dependent and pathway-specific.

Quantitative analysis of the percent buried volume and P–Ru–P bite angle against pyridine binding energies revealed that complexes with a $\%V_{\text{bur}}$ in the optimal range of 40–50% and P–Ru–P bite angles near 95–115° demonstrate improved substrate accessibility. These values define a "catalytic sweet spot," where steric bulk is sufficient to modulate substrate binding without imposing excessive geometric constraints that would hinder catalyst flexibility. In contrast, bulky substituents (*t*Bu, *i*Pr, Cy) with $\%V_{\text{bur}} > 55\%$ and P–Ru–P angles exceeding 115° consistently show poor performance across all pathways. The relationship between $\%V_{\text{bur}}$ and binding energy is quasi-linear in the fully coordinated regime but exhibits pronounced non-linearity in hemilabile pathways. This shift reflects a transition from purely steric control to a regime where geometric reorganization allows for conformational compensation.

The quantitative relationships established in this study may underpin rational catalyst design by translating mechanistic insights and descriptor analysis into targeted strategies for advancing future design implications in homogeneous pincer catalysis.

First, backbone selection could provide geometric tunability. For example, the choice between CH_2-linker systems (PNpyP, NNpyN) and O-linker systems (PONOP, NONpyON). CH_2-linker systems provide greater conformational flexibility and lower overall $\%V_{\text{bur}}$, making them suitable for catalytic applications requiring rapid intermediate dynamics or unusually bulky substrates. O-linker systems impose greater rigidity and steeper steric requirements but offer enhanced geometric definition and potential for more predictable binding modes. The observed correlation between backbone rigidity and isomeric preference suggests that O-linker systems may provide improved regioselectivity in asymmetric catalysis, warranting experimental validation.

Second, the evaluation of six distinct substituents reveals that no single substituent optimizes performance across all coordination pathways. Instead, the optimal substituent selection depends on the coordination pathway. For pathways where substrate binding occurs via nitrogen dissociation, phenyl and small alkyl substituents such as methyl offer improved binding energetics. For the coordination pathway involving phosphorus dissociation, smaller, planar substituents dominate, though cyclohexyl substituents may emerge as competitive. The near universal advantage of phenyl planar aromatic groups suggests that electronic interactions provide a generalizable stabilization across multiple pathways.

Third, the stabilization observed through π–π stacking between the pyridine substrate and the pyridine ring of the PNpyP pincer suggests that deliberate incorporation of lutidine-based bridges in pincer backbones coupled to catalytic metal centers represents a possible design strategy. The 55+ kJ/mol stabilization achieved through optimized aromatic alignment demonstrates that second-sphere interactions warrant equivalent consideration to first-sphere coordination chemistry.

Finally, given that many systems exhibit broad energy spans across conformer ensembles, and catalyst populations under realistic reaction conditions comprise multiple conformational isomers, rate-determining steps and selectivity must be understood as ensemble properties. Design strategies should therefore prioritize systems where the conformational ensemble maintains favorable properties across multiple accessible states, rather than depending on a single narrow optimum.

Future studies should focus more on the hemilability of the pincer donors, as the automated bias-free MACE computational workflow can be readily extended to screen larger chemical spaces. Systematic variation of pincer donor atoms (mixed N/P/S combinations) results in alternative lutidine backbones (PNpyN, SNpyS, NNpyN, NNpyS, PNpyS, SNpyN) and diverse substituents, enabling a comprehensive mapping of structure–property relationships across various architectures. This approach may potentially identify previously unexplored hemilabile systems with enhanced catalytic performance.

Furthermore, the quantitative predictions emerging from this work, particularly the hierarchy of binding pathway accessibility and the quantitative estimates of binding energies, should be experimentally validated through direct measurement of Gibbs free energies via NMR or spectroscopic titration experiments. Agreement between predicted and experimental values would validate the computational methodology and build confidence in predictions for systems not yet synthesised.

Additionally, the current work focuses on static structural properties and substrate binding thermodynamics. Extension to transition state geometries and activation barriers would complete the full catalytic cycle. DFT calculations of representative catalytic steps (e.g., C–H activation, hydrogenation, dehydrogenation) on selected complex architectures would reveal whether the predicted substrate binding advantages translate to catalytic rate enhancements.

While this work focuses predominantly on steric effects through percent buried volume and bite angle, a key limitation is the omission of explicit electronic descriptors. Incorporating electronic structure analysis in future studies, such as NBO-based donor–acceptor interactions, could quantify σ-donation and π-backdonation within the ruthenium pincer framework. HOMO/LUMO energies and gaps would help probe overall electrophilicity, nucleophilicity, and redox flexibility. Mayer bond orders for Ru–P and Ru–N bonds could measure bond strength and hemilability along the three coordination pathways. Finally, Mulliken charges on the metal center, donor atoms, and pyridine substrate would track charge distribution and ligand-to-metal or metal-to-ligand charge transfer upon binding. Together, these electronic descriptors, combined with steric parameters, would provide a more comprehensive assessment of how both factors cooperatively govern hemilability and pyridine binding in ruthenium pincer complexes.

A

Supplementary data

Table A.1: Relative Gibbs free energy differences between two isomers of $RuH_2(CO)(\kappa^3\text{-}R_2\text{-}LXN_{py}XL\text{-}R_2)$ pincer complexes, where $LXN_{py}XL$ = {$PN_{py}P$, $NN_{py}N$, $PON_{py}OP$, $NON_{py}ON$} and R = {Me, Bu, iPr, Ph, Cy, tBu}.

Backbone	**R**	$\Delta\Delta G_{\text{iso1-iso0}}$ **(kJ/mol)**
$PN_{py}P$	Me	14.60358235
	Bu	9.70631597
	iPr	11.19324164
	Ph	6.877418485
	Cy	6.60344756
	tBu	25.48872157
$PON_{py}OP$	Me	3.49044472
	Bu	5.783635185
	iPr	7.443056205
	Ph	2.309967411
	Cy	20.19749891
	tBu	12.94907102
$NON_{py}ON$	Me	15.43975159
	Bu	18.52694577
	iPr	11.46986432
	Ph	4.622061475
	Cy	−1.68735634
	tBu	12.46361607
$NN_{py}N$	Me	35.75962506
	Bu	19.77198412
	iPr	15.56283504
	Ph	18.70442957
	Cy	23.31570024
	tBu	41.89649501

Table A.2: Absolute Gibbs free energies of reference states for $RuH_2(CO)(\kappa^3\text{-PNP})$ pincer complexes with different R substituents (R = Me, Bu, tBu, iPr, Cy, Ph).

R	Δ*G* (kJ/mol)
Cy	-5658979.624
Ph	-5621686.925
Bu	-4847706.744
tBu	-4847664.271
iPr	-4435887.840
Me	-3612255.565

Table A.3: Absolute Gibbs free energies of pyridine and carbonyl ligands

ligand	Δ*G* (kJ/mol)
pyridine	-650485.421610435
carbonyl	-296971.42120507

Table A.4: Computed pyridine binding energies (ΔG_{bind}), percent buried volumes (V_{bur}), and P-Ru-P bite angles for the 11 lowest-energy conformers of substrate-specific pincer complexes ($RuH_2(py)(\kappa^3\text{-PNP})$, $RuH_2(CO)(\kappa^2\text{-P,N-PNP})(py)$, and $RuH_2(CO)(\kappa^2\text{-P,P-PNP})(py)$) across various substituents (R = Me, Bu, tBu, iPr, Cy, Ph).

Complex	R	Rank	ΔG_{bind} (kJ/mol)	V_{bur} (%)	P-Ru-P (°)
$RuH_2(py)(\kappa^3\text{-PNP})$	Me	1	130.266	54.6	163.212
		2	130.267	54.9	163.114
		3	130.410	54.8	163.364
		4	130.712	54.8	163.214
		5	130.756	54.8	163.152
		6	130.779	54.8	163.061
		7	130.834	54.8	163.222
		8	130.915	54.8	163.396
		9	131.068	54.9	163.438
		10	131.183	54.7	162.947
		11	131.280	54.7	163.293
	Bu	1	129.006	60.1	162.946
		2	129.651	58.8	162.912
		3	130.732	58.7	163.034
		4	132.059	58.9	163.326
		5	132.965	60.0	163.156
		6	133.618	60.2	162.777
		7	133.787	57.5	166.505
		8	133.862	59.6	163.773
		9	133.924	58.5	162.988
		10	135.098	60.4	163.697
		11	135.608	61.2	163.239
	iPr	1	138.068	63.6	162.902
		2	139.490	63.7	162.894
		3	140.570	63.8	160.085
		4	141.083	63.5	162.864
		5	143.683	64.3	161.263
		6	144.197	64.6	162.722

Continued on next page

Table A.4 – *Continued from previous page*

Complex	**R**	**Rank**	$\Delta G_{\mathbf{bind}}$ **(kJ/mol)**	$V_{\mathbf{bur}}$ **(%)**	**P-Ru-P (°)**
		7	144.475	63.8	161.371
		8	144.780	64.5	162.638
		9	145.628	64.0	162.786
		10	146.210	63.5	163.089
		11	146.952	63.4	160.013
	Ph	1	104.969	61.6	163.614
		2	105.341	61.5	163.317
		3	105.506	61.6	163.370
		4	105.942	61.6	163.420
		5	106.748	61.7	163.133
		6	106.752	61.7	163.141
		7	106.890	61.5	163.590
		8	106.934	61.7	163.416
		9	106.936	61.4	163.437
		10	106.954	61.7	163.103
		11	106.991	61.6	163.129
	Cy	1	124.918	65.8	160.376
		2	138.354	63.7	163.705
		3	139.815	67.0	160.690
		4	140.633	65.4	163.904
		5	141.400	64.1	160.600
		6	142.237	65.5	163.359
		7	146.836	62.4	162.922
		8	147.113	64.8	164.240
		9	148.958	65.6	162.093
		10	151.433	65.4	159.808
		11	152.262	63.4	164.063
	tBu	1	151.629	69.1	164.281
		2	152.492	69.1	164.372
		3	152.645	69.4	164.440
		4	153.138	69.2	164.593
		5	153.481	68.5	156.501
		6	153.667	69.0	164.132
		7	153.712	68.5	156.274
		8	153.778	68.6	156.397
		9	153.803	68.7	157.576
		10	153.817	69.2	164.111
		11	153.896	69.3	164.476
$RuH_2(CO)(\kappa^2$-P,N-PNP)(py)	Me	1	136.109	40.8	85.289
		2	137.467	41.2	85.380
		3	133.344	42.1	89.389
		4	106.358	41.4	89.436
		5	125.646	39.4	91.092
		6	125.413	39.0	96.249
		7	129.878	40.8	100.017
		8	106.005	41.2	100.541
		9	102.884	41.5	101.707
		10	134.354	41.0	103.317
		11	101.000	41.6	106.095

Continued on next page

Table A.4 – *Continued from previous page*

Complex	R	Rank	ΔG_{bind} (kJ/mol)	V_{bur} (%)	P-Ru-P (°)
	Bu	1	87.962	46.0	132.700
		2	95.036	42.1	125.125
		3	96.692	42.1	108.046
		4	97.396	46.6	108.214
		5	105.793	44.7	114.350
		6	106.182	44.8	126.660
		7	107.950	44.0	133.757
		8	111.281	40.9	127.033
		9	111.898	41.8	109.688
		10	112.997	41.2	127.465
		11	113.726	41.9	119.795
	iPr	1	105.980	46.8	136.126
		2	108.210	46.8	101.167
		3	112.798	44.1	125.826
		4	114.013	44.7	130.397
		5	114.573	46.9	105.217
		6	114.585	44.0	123.613
		7	121.899	42.9	117.422
		8	124.217	44.6	120.211
		9	124.611	46.2	102.163
		10	125.378	45.6	112.667
		11	126.652	45.4	103.602
	Ph	1	60.333	43.7	113.732
		2	62.023	45.9	137.417
		3	67.346	44.9	105.555
		4	68.865	44.1	128.970
		5	69.022	43.4	130.607
		6	78.349	45.7	115.431
		7	79.931	41.7	115.648
		8	80.608	44.1	127.138
		9	82.588	45.7	113.651
		10	86.662	42.2	116.752
		11	87.293	46.5	126.000
	Cy	1	74.974	47.7	129.438
		2	91.918	45.8	102.108
		3	96.603	47.1	134.103
		4	103.567	43.6	115.847
		5	114.896	44.4	127.014
		6	127.129	46.1	91.140
		7	132.312	45.7	115.711
		8	132.529	46.5	109.306
		9	136.718	48.3	142.179
		10	144.484	44.5	125.625
		11	145.870	48.3	144.968
	tBu	1	102.085	50.0	138.571
		2	102.720	48.5	130.485
		3	105.413	48.6	117.641
		4	105.952	49.0	137.136
		5	109.775	50.1	139.577

Continued on next page

Table A.4 – *Continued from previous page*

Complex	**R**	**Rank**	$\Delta G_{\mathbf{bind}}$ **(kJ/mol)**	$V_{\mathbf{bur}}$ **(%)**	**P-Ru-P (°)**
		6	110.844	48.9	116.657
		7	110.940	48.0	127.868
		8	111.406	48.5	122.375
		9	118.650	49.4	112.467
		10	119.345	46.7	129.009
		11	120.762	48.2	125.971
$RuH_2(CO)(\kappa^2$-P,P-PNP)(py)	Me	1	39.339	44.3	100.024
		2	42.538	44.3	110.632
		3	53.485	44.0	98.598
		4	60.223	43.7	98.363
		5	61.091	44.4	109.261
		6	65.325	44.9	98.613
		7	68.231	45.5	108.750
		8	72.631	44.9	103.722
		9	75.383	44.4	98.289
		10	83.064	44.1	96.925
		11	92.397	43.6	100.703
	Bu	1	45.864	48.2	100.868
		2	53.513	49.2	111.807
		3	56.971	47.8	99.449
		4	62.268	47.3	109.196
		5	67.871	49.6	109.201
		6	69.676	48.9	103.000
		7	75.953	48.7	103.396
		8	87.558	52.4	104.345
		9	100.616	47.8	100.676
		10	101.400	49.5	97.824
		11	106.714	48.2	99.668
	iPr	1	95.188	52.0	103.507
		2	97.194	52.6	108.184
		3	102.851	51.9	103.393
		4	110.432	51.0	100.238
		5	116.627	53.6	106.504
		6	119.964	50.9	106.597
		7	122.054	53.0	104.755
		8	134.996	54.3	105.250
		9	142.548	51.0	105.705
		10	146.895	49.8	99.778
		11	156.385	51.5	103.460
	Ph	1	29.888	75.8	99.317
		2	47.421	75.0	112.555
		3	49.009	79.4	110.298
		4	51.325	76.2	101.463
		5	52.686	76.0	97.728
		6	55.351	77.1	98.444
		7	61.295	77.2	98.399
		8	61.628	77.8	104.781
		9	67.737	76.3	105.271
		10	75.840	77.8	103.360

Continued on next page

Table A.4 – *Continued from previous page*

Complex	**R**	**Rank**	$\Delta G_{\mathbf{bind}}$ **(kJ/mol)**	$V_{\mathbf{bur}}$ **(%)**	**P-Ru-P (°)**
		11	82.860	79.3	98.717
	Cy	1	88.697	51.0	101.573
		2	88.855	54.1	109.814
		3	102.711	51.8	104.632
		4	116.156	53.1	120.629
		5	120.815	51.8	103.171
		6	126.354	54.4	102.441
		7	132.256	53.2	107.114
		8	142.492	53.5	109.418
		9	156.224	52.8	101.075
		10	173.780	50.3	101.333
		11	175.344	52.0	102.413
	tBu	1	125.521	82.8	115.016
		2	130.052	79.2	112.192
		3	132.726	79.6	112.122
		4	143.143	77.4	111.188
		5	149.367	78.4	116.524
		6	159.852	81.9	110.453
		7	161.431	80.3	110.002
		8	167.471	79.9	109.320
		9	182.776	82.3	113.040
		10	187.710	77.4	116.751
		11	203.449	77.4	107.270

B

Supporting figures

B.1 UFF based conformational energy analysis of $RuH_2(CO)(\kappa^3$-Pincer) across various backbones and substituents

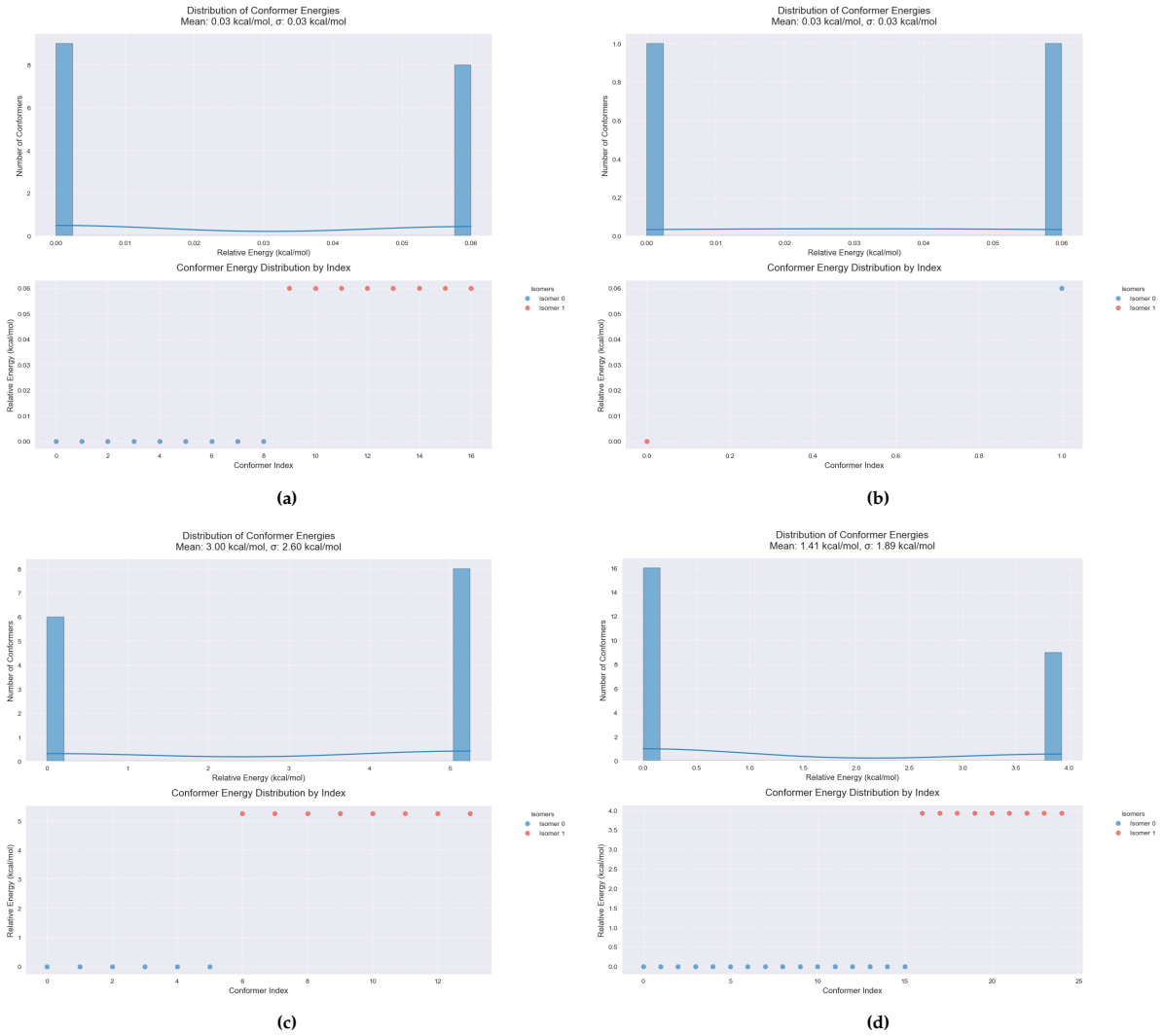

Figure B.1: Scatter plots and histograms visualizing the conformational energy distributions of methyl-substituted $RuH_2(CO)(\kappa^3$-pincer) across different ligand backbones. (a) PNpyP, (b) NNpyN, (c) NONpyON, and (d) PONpyOP. All conformer energies are computed using the Universal Force Field.

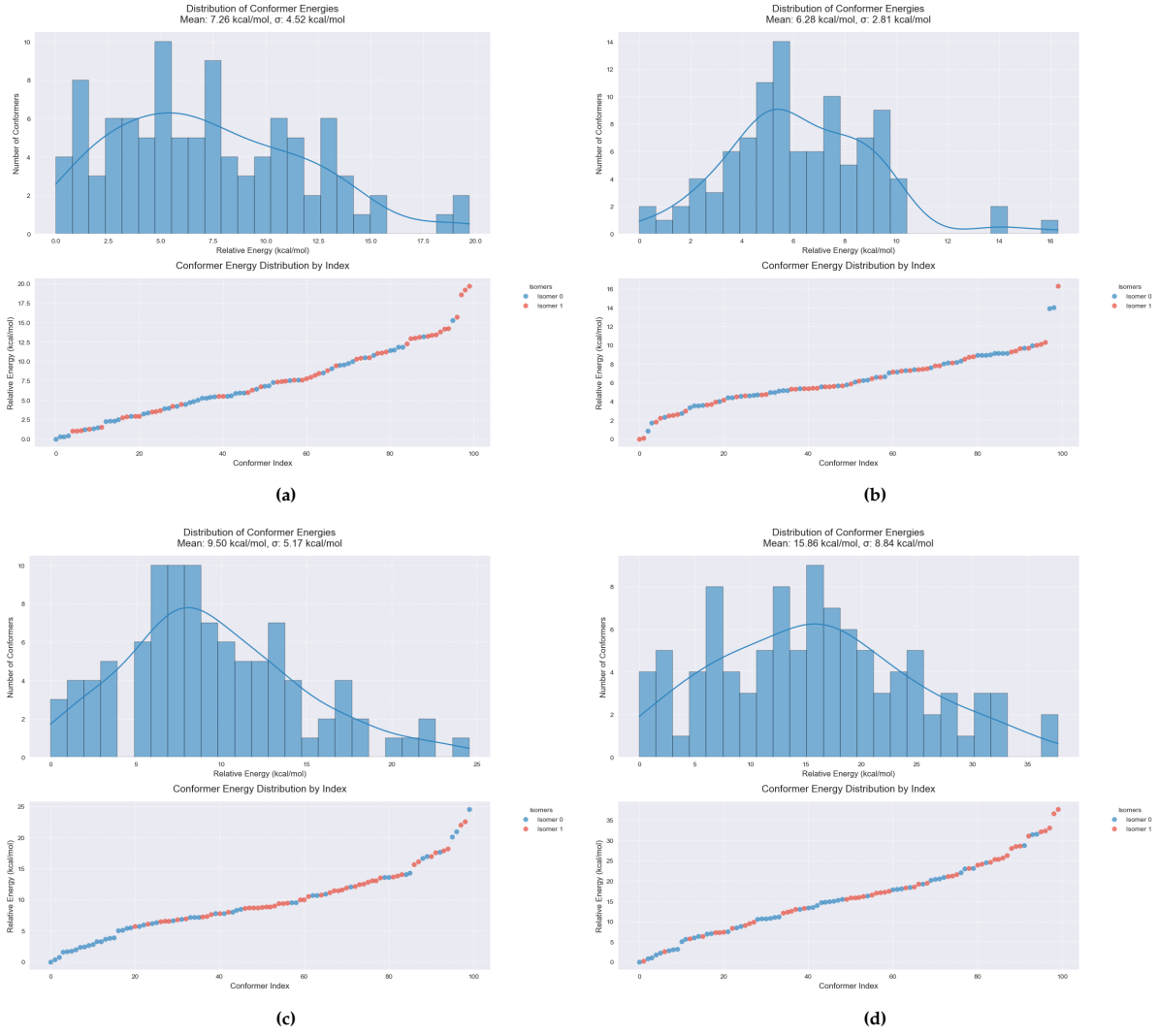

Figure B.2: Scatter plots and histograms visualizing the conformational energy distributions of butyl-substituted $RuH_2(CO)(\kappa^3$-pincer) across different ligand backbones. (a) PNpyP, (b) NNpyN, (c) NONpyON, and (d) PONpyOP. All conformer energies are computed using the Universal Force Field.

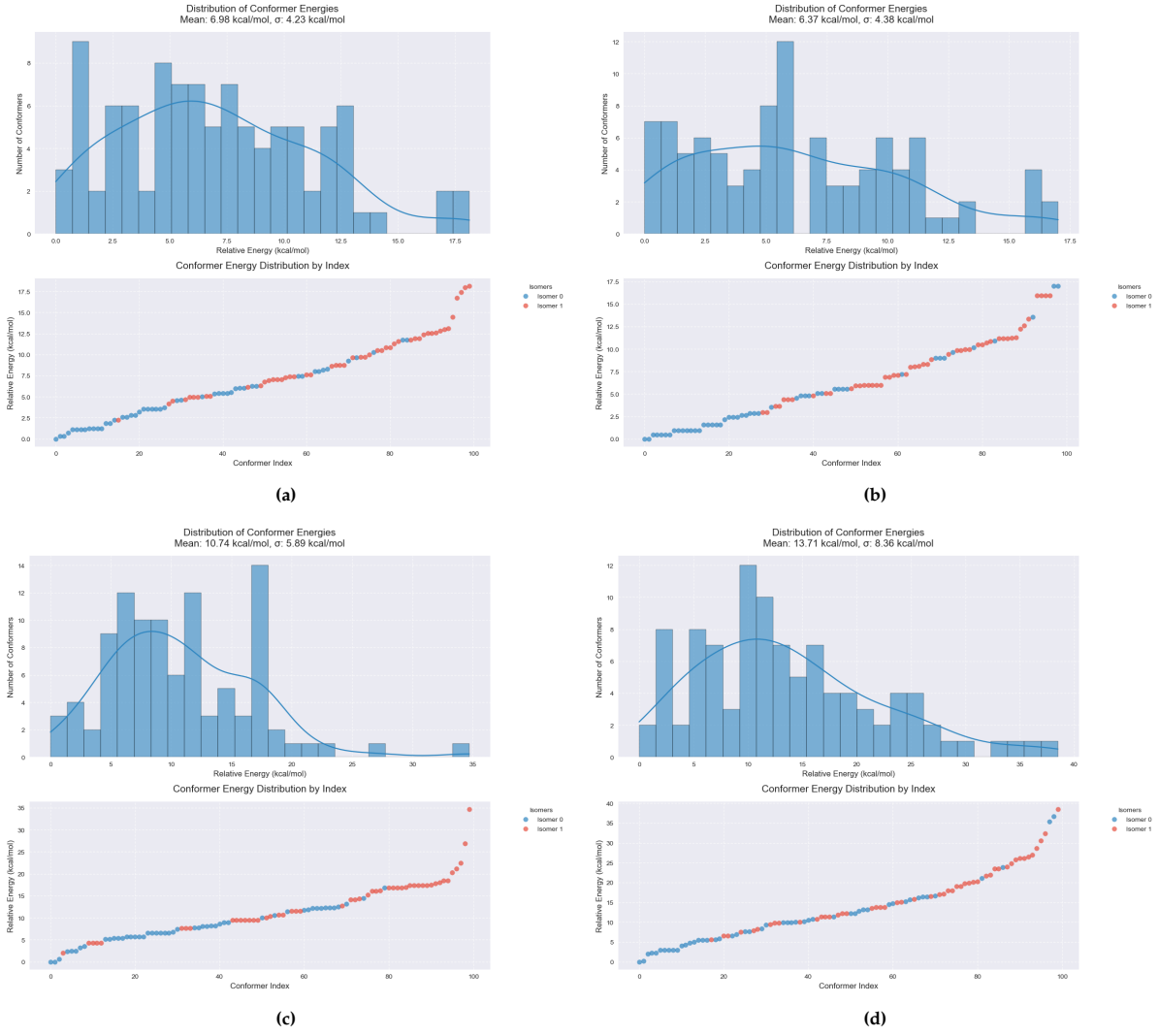

Figure B.3: Scatter plots and histograms visualizing the conformational energy distributions of isopropyl-substituted $RuH_2(CO)(\kappa^3$-pincer) across different ligand backbones. (a) PNpyP, (b) NNpyN, (c) NONpyON, and (d) PONpyOP. All conformer energies are computed using the Universal Force Field.

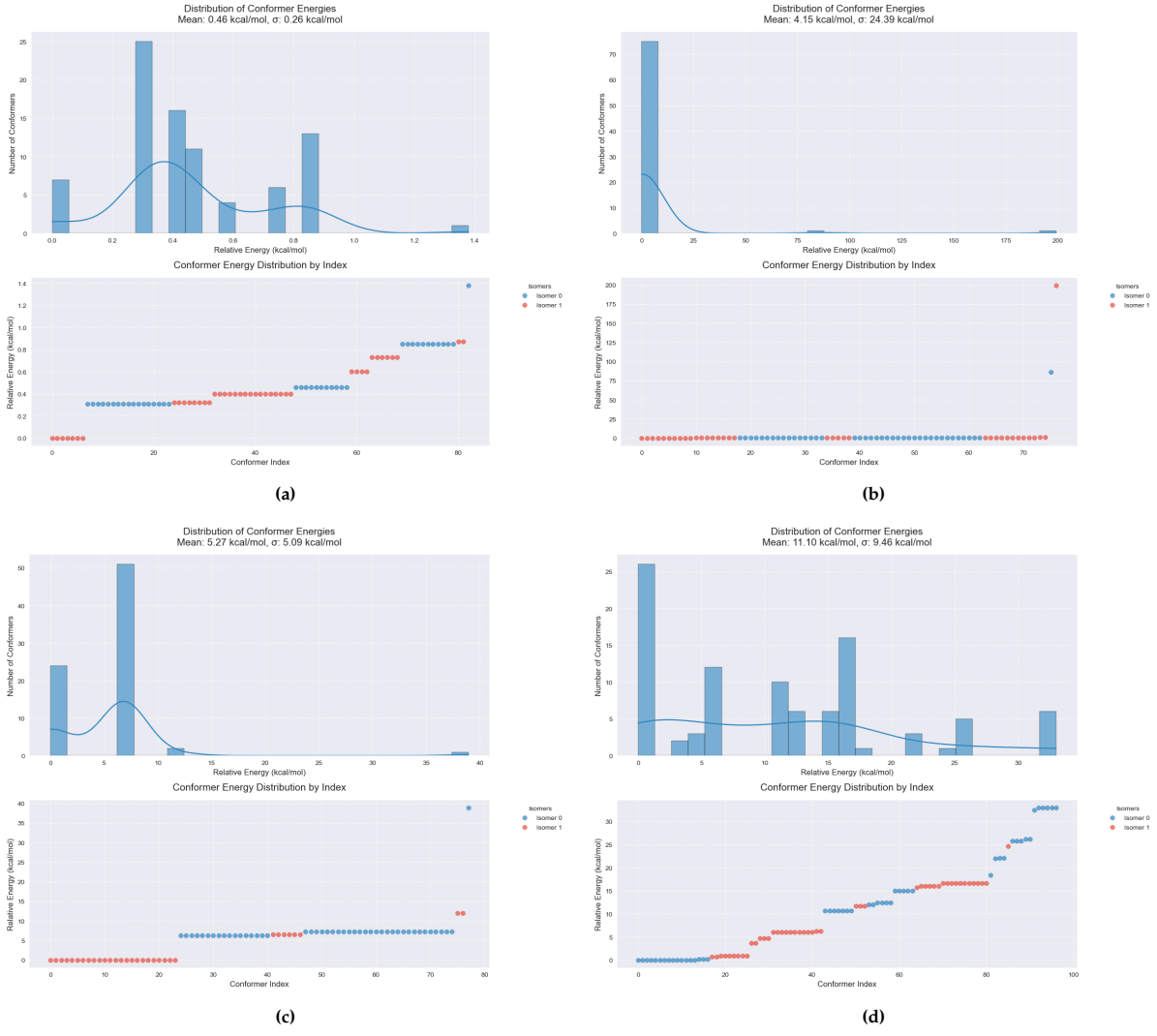

Figure B.4: Scatter plots and histograms visualizing the conformational energy distributions of phenyl-substituted $RuH_2(CO)(\kappa^3$-pincer) across different ligand backbones. (a) PNpyP, (b) NNpyN, (c) NONpyON, and (d) PONpyOP. All conformer energies are computed using the Universal Force Field.

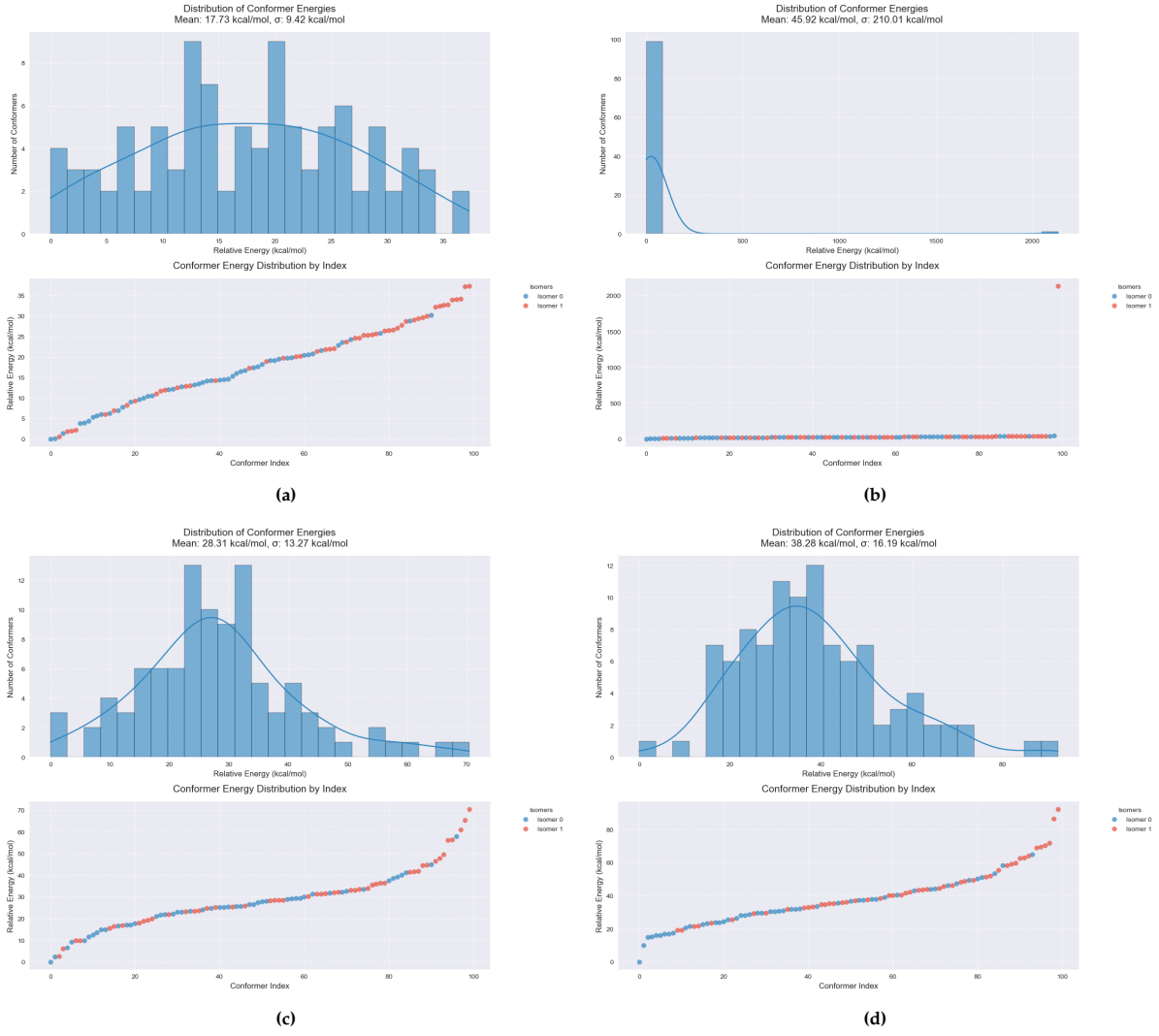

Figure B.5: Scatter plots and histograms visualizing the conformational energy distributions of cyclohexyl-substituted $RuH_2(CO)(\kappa^3$-pincer) across different ligand backbones. (a) PNpyP, (b) NNpyN, (c) NONpyON, and (d) PONpyOP. All conformer energies are computed using the Universal Force Field.

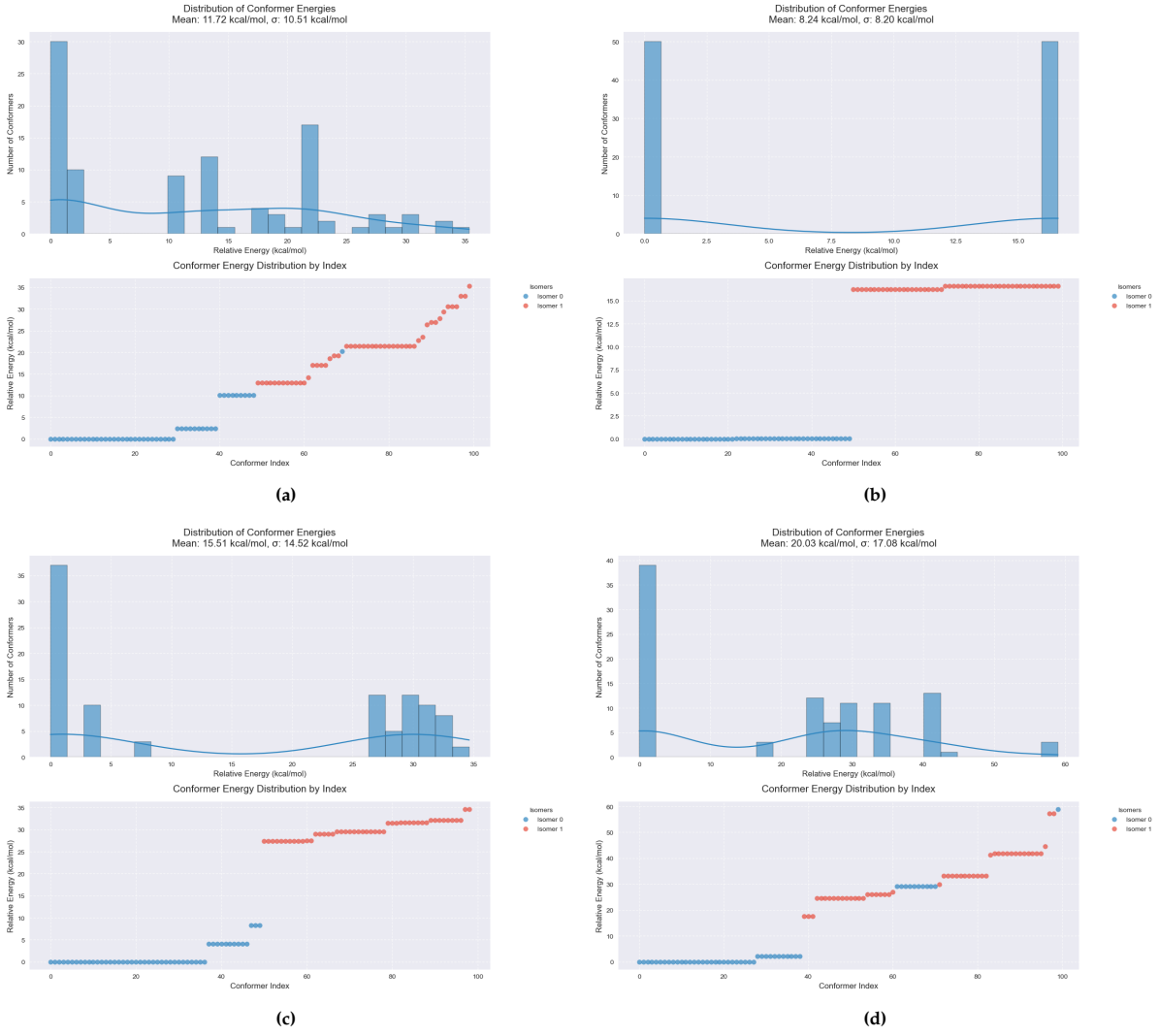

Figure B.6: Scatter plots and histograms visualizing the conformational energy distributions of tert-butyl-substituted $RuH_2(CO)(\kappa^3$-pincer) across different ligand backbones. (a) PNpyP, (b) NNpyN, (c) NONpyON, and (d) PONpyOP. All conformer energies are computed using the Universal Force Field.

B.2 Pyridine binding free energy vs. steric descriptors for $RuH_2(py)(\kappa^3\text{-PNP})$, $RuH_2(CO)(\kappa^2\text{-P,N-PNP})(py)$ and $RuH_2(CO)(\kappa^2\text{-P,P-PNP})(py)$

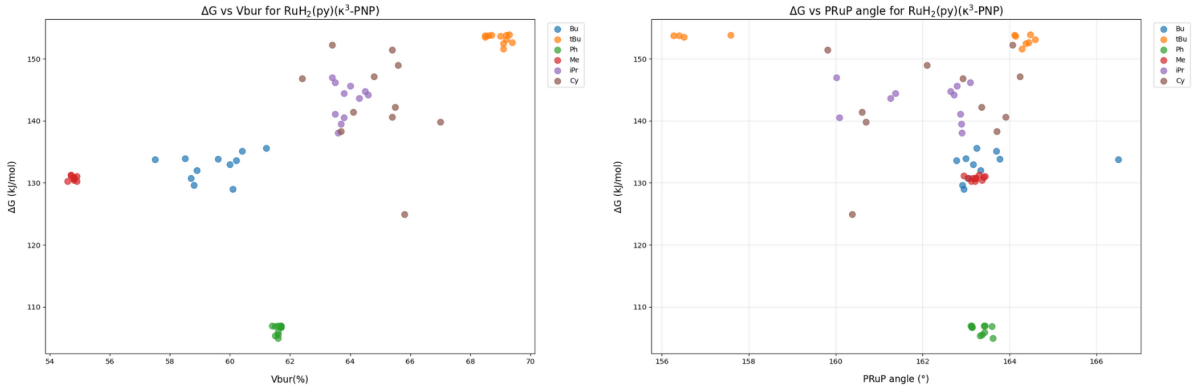

(a) (b)

Figure B.7: Scatter plots showing the relationship between pyridine binding free energy (ΔG, kJ/mol) and steric descriptors for $RuH_2(py)(\kappa^3\text{-PNP})$ complex across various substituents (Me, Bu, iPr, tBu, Cy, and Ph). (a) Pyridine binding free energy (ΔG, kJ/mol) versus percent buried volume ($\%V_{bur}$). (b) Pyridine binding free energy (ΔG, kJ/mol) versus P–Ru–P bite angle (°).

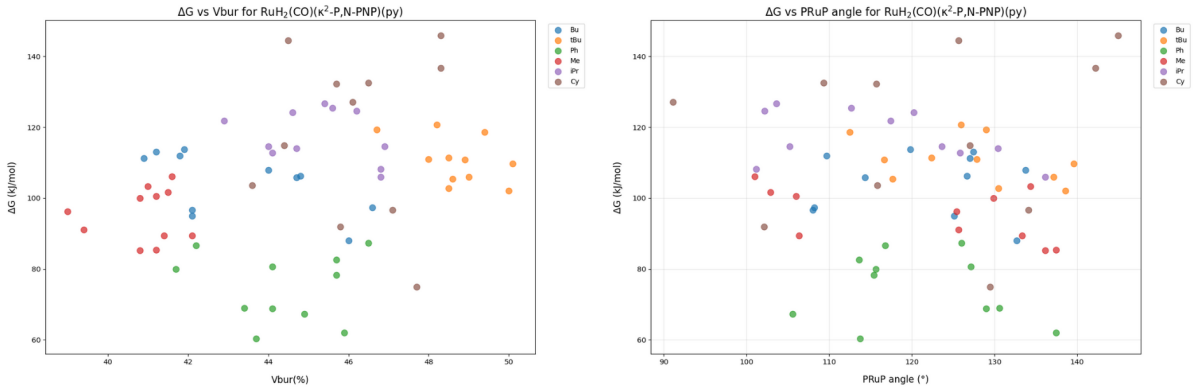

(a) (b)

Figure B.8: Scatter plots showing the relationship between pyridine binding free energy (ΔG, kJ/mol) and steric descriptors for $RuH_2(CO)(\kappa^2\text{-P,N-PNP})(py)$ complex across various substituents (Me, Bu, iPr, tBu, Cy, and Ph). (a) Pyridine binding free energy (ΔG, kJ/mol) versus percent buried volume ($\%V_{bur}$). (b) Pyridine binding free energy (ΔG, kJ/mol) versus P–Ru–P bite angle (°).

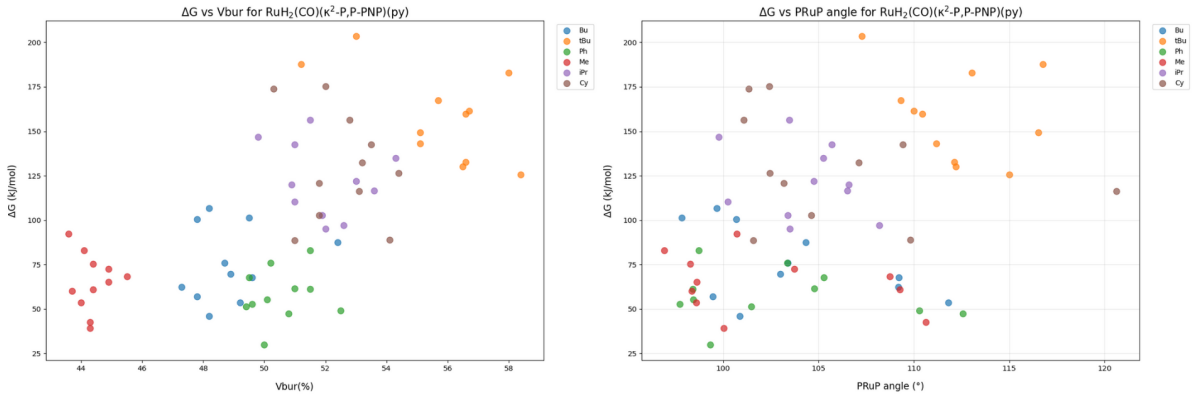

(a) (b)

Figure B.9: Scatter plots showing the relationship between pyridine binding free energy (ΔG, kJ/mol) and steric descriptors for $RuH_2(CO)(\kappa^2$-P,P-PNP)(py) complex across various substituents (Me, Bu, iPr, tBu, Cy, and Ph). (a) Pyridine binding free energy (ΔG, kJ/mol) versus percent buried volume ($\%V_{bur}$). (b) Pyridine binding free energy (ΔG, kJ/mol) versus P–Ru–P bite angle (°).

C

DFT-optimised structures

C.1 Optimised structures of $RuH_2(CO)(\kappa^3$-PNP) reference complexes

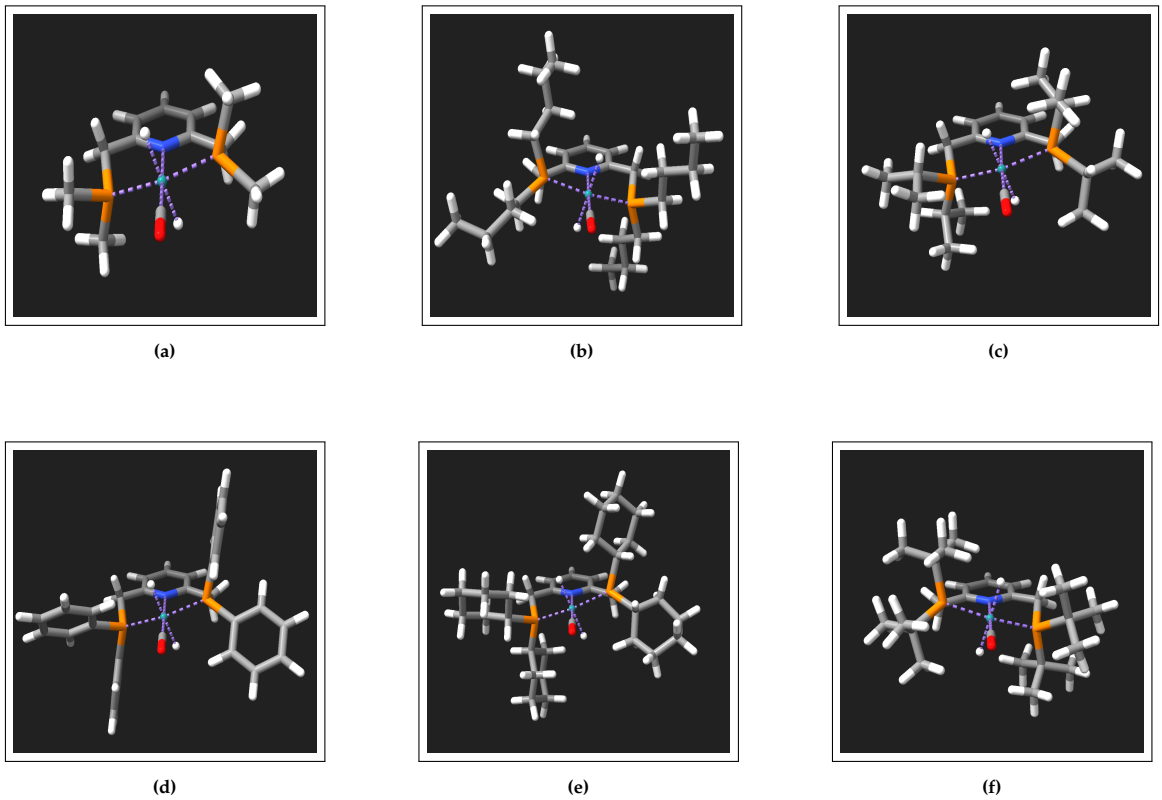

Figure C.1: Optimized structures of $RuH_2(CO)(\kappa^3$-PNP) reference complexes.

C.2 Optimised substrate-specific complexes

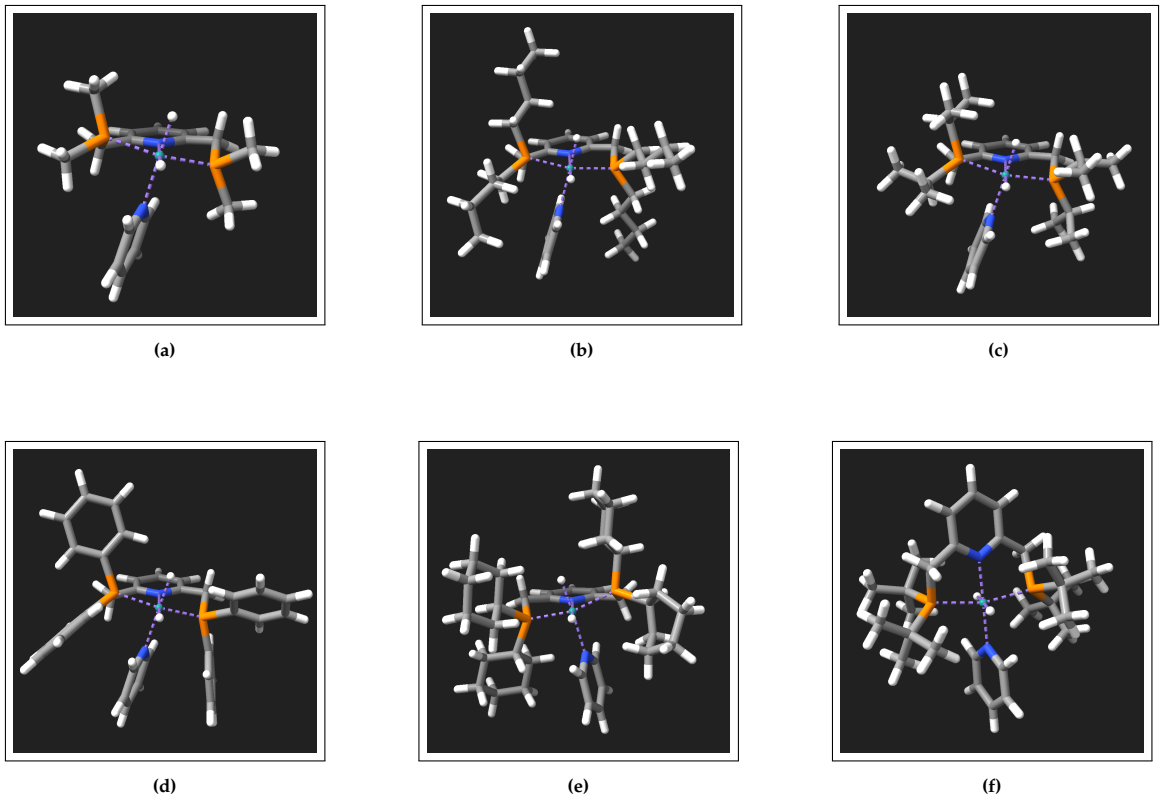

Figure C.2: Optimised structures of $RuH_2(py)(\kappa^3\text{-PNP})$ complexes.

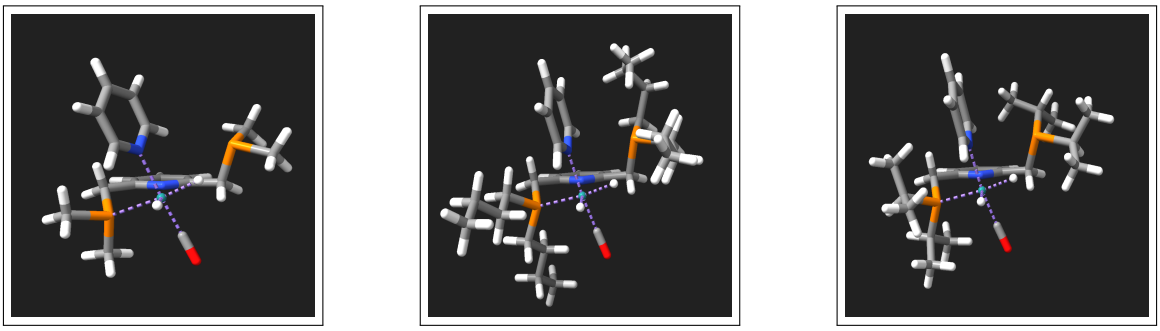

(a) (b) (c)

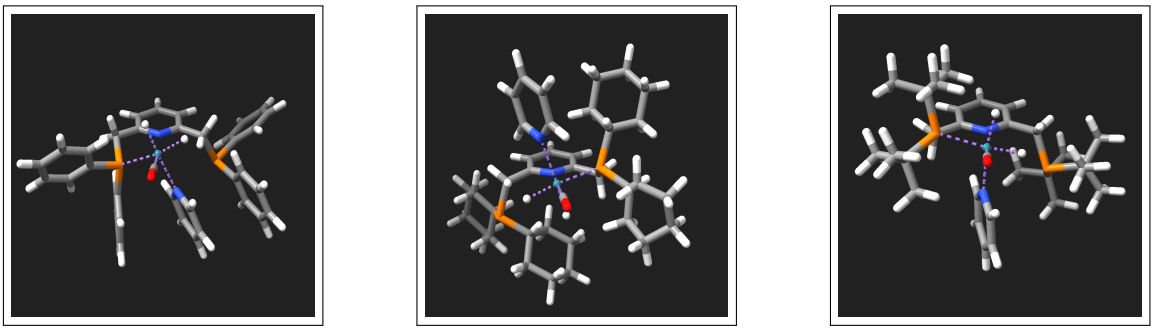

(d) (e) (f)

Figure C.3: Optimised structures of $RuH_2(CO)(\kappa^2$-P,N-PNP)(py) complexes.

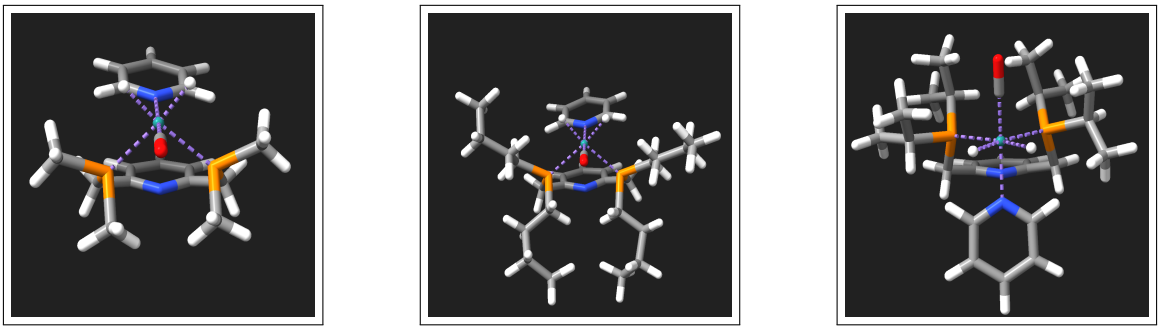

(a) (b) (c)

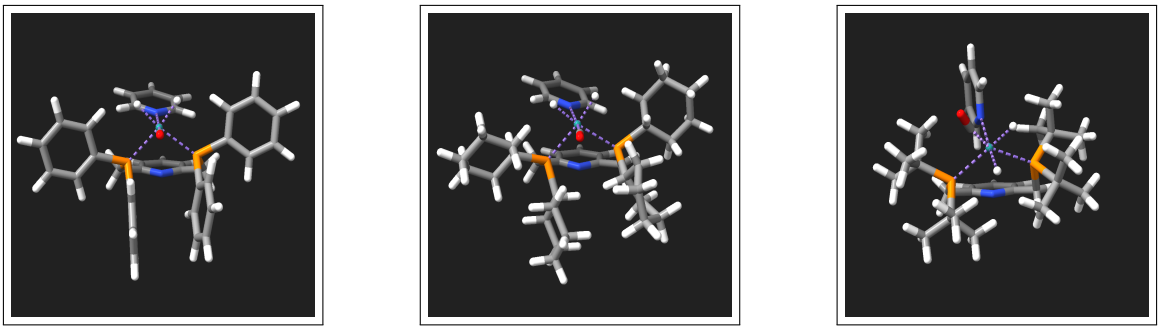

(d) (e) (f)

Figure C.4: Optimised structures of $RuH_2(CO)(\kappa^2$-P,P-PNP)(py) complexes.

D

Declaration of AI use

While writing this report, I used the following LLM models to assist in the process:

Overview

LLM model	Use
Perplexity	Literature review
Gemini 2.5 pro/Gemini 3 pro	Language refinement
Goblin Tools Formalizer	Language refinement
Grammarly	Spelling and grammar check
ChatGPT-4o	LaTeX code refinement
Github Copilot	Code assistance

Literature review

I often get lost in literature when I want to delve deeper into a particular subject. Search engines, such as Google, overwhelm you with information, making it difficult to distinguish what is relevant from what is not. I find it challenging to establish clear boundaries on what I should and should not read. I used Perplexity to search for specific information and sources relevant for further exploration, which allowed me to work more focused and save time.

Language refinement

I often struggle to formulate cohesive sentences that clearly convey my ideas. I used the Goblin Tools Formalizer to help me construct complete sentences from my initial fragmented thoughts. Additionally, my sentences often have complicated structures, which are long and unclear, and contain abstract language. I have used Gemini 2.5 pro and Gemini 3 pro to maintain a consistent writing style in longer texts by simplifying complicated sentence structures and improving the overall readability of my text by:

- Removing unnecessary words, adverbs, and subordinate clauses.
- Clarifying vague formulations and abstract language and making them more concrete with suggestions and examples that can clarify abstract concepts.
- Splitting long sentences into shorter, clearer parts and using connecting words more consistently.

LaTeX code refinement

I used ChatGPT-4o for LaTeX code refinement in the following ways:

- Identifying and correcting syntax issues.
- Reorganising code to improve clarity and structure.
- Applying consistent formatting, including indentation and spacing.
- Improving page layout, such as captions, figures, and tables.
- Converting text-based mathematical expressions into properly formatted LaTeX.

Code assistance

I used GitHub Copilot as a coding assistant integrated into Visual Studio Code in the following ways:

- Explaining code and answering technical questions in the chat.
- Suggesting code completions.
- Debugging, fixing errors, and recommending corrections.

Reflection

AI is an advanced language model that recognises patterns and generates responses based on predictions. It operates on probability rather than actual knowledge, which made it important for me to think critically about the responses it generated. I primarily used LLMs as sparring partners to help me reflect, think critically, and explore broader perspectives on my content, views, and thoughts, rather than seeing them as a source of information. By focusing on the suggestions they offered, rather than blindly trusting the generated answers, they served primarily as tools to stimulate my own thought process while developing content that remained inherently my own. This gave me an additional lens through which to critically examine my writing style, phrasing, and reasoning. It helped me gain deeper insight into how my writing was structured and which aspects I could improve. By viewing LLMs not as a source of information but purely as sparring partners in the writing process, I was able to strengthen my thinking and further develop my writing skills.

Bibliography

[1] Chenyang Chu et al. "Hydrogen Storage by Liquid Organic Hydrogen Carriers: Catalyst, Renewable Carrier, and Technology – A Review". In: *Carbon Resources Conversion* 6.4 (Mar. 21, 2023), pp. 334–351. DOI: 10.1016/j.crcon.2023.03.007. URL: https://doi.org/10.1016/j.crcon.2023.03.007.

[2] Min-Jie Zhou et al. "Recent Advances in Reversible Liquid Organic Hydrogen Carrier Systems: From Hydrogen Carriers to Catalysts". In: *Advanced Materials* 36.37 (Feb. 20, 2024), e2311355. DOI: 10.1002/adma.202311355. URL: https://doi.org/10.1002/adma.202311355.

[3] Gerardo Cabrera et al. "Liquid Organic Hydrogen Carrier Concepts and Catalysts for Hydrogenation and Dehydrogenation Reactions". In: *Molecules* 29.20 (Oct. 18, 2024), p. 4938. DOI: 10.3390/molecules29204938. URL: https://pmc.ncbi.nlm.nih.gov/articles/PMC11510432/.

[4] J. Steinhauer et al. "Model Catalytic Studies of Liquid Organic Hydrogen Carriers: Indole/Indoline/Octahydroindole on Ni(111)". In: *The Journal of Physical Chemistry C* 124.41 (Sept. 2020), pp. 22559–22567. DOI: 10.1021/acs.jpcc.0c06988. URL: https://doi.org/10.1021/acs.jpcc.0c06988.

[5] Andy Lin and Giuseppe Bagnato. "Revolutionising Energy Storage: The Latest Breakthrough in Liquid Organic Hydrogen Carriers". In: *International Journal of Hydrogen Energy* 63 (Mar. 19, 2024), pp. 315–329. DOI: 10.1016/j.ijhydene.2024.03.146. URL: https://doi.org/10.1016/j.ijhydene.2024.03.146.

[6] Juwon Paik et al. "Thermodynamic Hydricity of a Ruthenium CO_2 Hydrogenation Catalyst Supported by a Rigid PNP Pincer". In: *JACS Au* 5.2 (Jan. 21, 2025), pp. 811–821. DOI: 10.1021/jacsau.4c01078. URL: https://pmc.ncbi.nlm.nih.gov/articles/PMC11862944/.

[7] Georgy Filonenko. "On the Catalytic Hydrogenation of CO_2 and Carboxylic Acid Esters". Technische Universiteit Eindhoven, Jan. 1, 2015.

[8] Georgy A. Filonenko et al. "Highly Efficient Reversible Hydrogenation of Carbon Dioxide to Formates Using a Ruthenium PNP-Pincer Catalyst". In: *ChemCatChem* 6.6 (Apr. 17, 2014), pp. 1526–1530. DOI: 10.1002/cctc.201402119. URL: https://doi.org/10.1002/cctc.201402119.

[9] Georgy A. Filonenko et al. "Catalytic Hydrogenation of CO_2 to Formates by a Lutidine-Derived Ru–CNC Pincer Complex: Theoretical Insight into the Unrealized Potential". In: *ACS Catalysis* 5.2 (Jan. 9, 2015), pp. 1145–1154. DOI: 10.1021/cs501990c. URL: https://research.wur.nl/en/publications/catalytic-hydrogenation-of-cosub2sub-to-formates-by-a-lutidine-de.

[10] Georgy A. Filonenko et al. "The Impact of Metal–Ligand Cooperation in Hydrogenation of Carbon Dioxide Catalyzed by Ruthenium PNP Pincer". In: *ACS Catalysis* 3.11 (Oct. 4, 2013), pp. 2522–2526. DOI: 10.1021/cs4006869. URL: https://doi.org/10.1021/cs4006869.

[11] Ivan Yu. Chernyshov and Evgeny A. Pidko. "MACE: Automated Assessment of Stereochemistry of Transition Metal Complexes and Its Applications in Computational Catalysis". In: *Journal of Chemical Theory and Computation* 20.5 (Feb. 16, 2024), pp. 2313–2320. DOI: 10.1021/acs.jctc.3c01313. URL: https://doi.org/10.1021/acs.jctc.3c01313.

[12] Veronika Juraskova et al. "Modelling Ligand Exchange in Metal Complexes with Machine Learning Potentials". In: *Faraday Discussions* 256.0 (Aug. 2, 2024), pp. 156–176. DOI: 10.1039/d4fd00140k. URL: https://pmc.ncbi.nlm.nih.gov/articles/PMC11417676/.

[13] Arseniy A. Otlyotov et al. "16OSTM10: A New Open-Shell Transition Metal Conformational Energy Database to Challenge Contemporary Semiempirical and Force Field Methods". In: *Physical Chemistry Chemical Physics* 24.28 (Jan. 1, 2022), pp. 17314–17322. DOI: 10.1039/d2cp01659a. URL: https://pubs.rsc.org/en/content/articlehtml/2022/cp/d2cp01659a.

[14] Sylwia Kostera, Gabriele Manca, and Luca Gonsalvi. "Carbon Dioxide Hydrogenation to Formate Catalyzed by a Neutral, Coordinatively Saturated Tris-Carbonyl Mn(I)-PNP Pincer-Type Complex". In: *Chemistry – A European Journal* 29.70 (Sept. 18, 2023), e202302642. DOI: 10.1002/chem.202302642. URL: https://doi.org/10.1002/chem.202302642.

[15] Brittany J. Barrett and Vlad M. Iluc. "Coordination of a Hemilabile Pincer Ligand with an Olefinic Backbone to Mid-to-Late Transition Metals". In: *Inorganic Chemistry* 53.14 (June 24, 2014), pp. 7248–7259. DOI: 10.1021/ic500549z. URL: https://doi.org/10.1021/ic500549z.

[16] Gemma M. Adams and Andrew S. Weller. "POP-Type Ligands: Variable Coordination and Hemilabile Behaviour". In: *Coordination Chemistry Reviews* 355 (Sept. 2, 2017), pp. 150–172. DOI: 10.1016/j.ccr.2017.08.004. URL: https://doi.org/10.1016/j.ccr.2017.08.004.

[17] Kevin Schlenker et al. "Role of Ligand-Bound CO_2 in the Hydrogenation of CO_2 to Formate with a (PNP)Mn Catalyst". In: *ACS Catalysis* 11.13 (June 23, 2021), pp. 8358–8369. DOI: 10.1021/acscatal.1c01709. URL: https://doi.org/10.1021/acscatal.1c01709.

[18] Ilia Kevlishvili, Chenru Duan, and Heather J. Kulik. *Classification of Hemilabile Ligands Using Machine Learning*. 2023. URL: https://doi.org/10.26434/chemrxiv-2023-66jqr-v2.

[19] A. K. Rappe et al. "UFF, a full periodic table force field for molecular mechanics and molecular dynamics simulations". In: *Journal of the American Chemical Society* 114.25 (Dec. 1, 1992), pp. 10024–10035. DOI: 10.1021/ja00051a040. URL: https://doi.org/10.1021/ja00051a040.

[20] Naoki Narita et al. *Supplementary Information of a Dodecamethoxy[6]Cycloparaphenylene Consisting Entirely of Hydroquinone Ethers: Unveiling In-plane Aromaticity Through a Rotaxane Structure*.

[21] Laura Falivene et al. "Towards the online computer-aided design of catalytic pockets". In: *Nature Chemistry* 11.10 (Sept. 2, 2019), pp. 872–879. DOI: 10.1038/s41557-019-0319-5. URL: https://doi.org/10.1038/s41557-019-0319-5.

[22] Albert Poater et al. "SambVca: A Web Application for the Calculation of the Buried Volume of N-Heterocyclic Carbene Ligands". In: *European Journal of Inorganic Chemistry* 2009.13 (Feb. 27, 2009), pp. 1759–1766. DOI: 10.1002/ejic.200801160. URL: https://doi.org/10.1002/ejic.200801160.

[23] Anthony J. Schaefer, Victoria M. Ingman, and Steven E. Wheeler. "SEQCROW: A ChimeraX bundle to facilitate quantum chemical applications to complex molecular systems". In: *Journal of Computational Chemistry* 42.24 (June 9, 2021), pp. 1750–1754. DOI: 10.1002/jcc.26700. URL: https://doi.org/10.1002/jcc.26700.

[24] Mark Stradiotto and Rylan J. Lundgren. *Ligand design in metal chemistry. Reactivity and Catalysis*. John Wiley & Sons, Oct. 17, 2016.

[25] Frank Neese et al. "The ORCA quantum chemistry program package". In: *The Journal of Chemical Physics* 152.22 (June 12, 2020). DOI: 10.1063/5.0004608. URL: https://doi.org/10.1063/5.0004608.

[26] Kim Sharp and Franz Matschinsky. "Translation of Ludwig Boltzmann's Paper "On the Relationship between the Second Fundamental Theorem of the Mechanical Theory of Heat and Probability Calculations Regarding the Conditions for Thermal Equilibrium"". In: *Entropy* 17.4 (Apr. 2, 2015), pp. 1971–2009. DOI: 10.3390/e17041971. URL: https://doi.org/10.3390/e17041971.

[27] Daniel V. Schroeder. *An Introduction to Thermal Physics*. Oxford University Press, 2021.

[28] *Command line interface — epic-mace 0.5.0 documentation*. URL: https://epic-mace.readthedocs.io/en/latest/source/cli.html.

[29] Wikipedia contributors. *Arithmetic mean*. June 28, 2025. URL: https://en.wikipedia.org/wiki/Arithmetic_mean.

[30] Wolfram Research, Inc. *Standard Deviation – from Wolfram MathWorld*. URL: https://mathworld.wolfram.com/StandardDeviation.html.

[31] Wikipedia contributors. *Kernel density estimation*. Aug. 9, 2025. URL: https://en.wikipedia.org/wiki/Kernel_density_estimation.

[32] *Snellius: de Nationale Supercomputer*. URL: https://www.surf.nl/diensten/rekenen/snellius-de-nationale-supercomputer.

[33] Schrödinger, LLC. *PyMOL Open-Source Foundation on GitHub*. URL: https://github.com/schrodinger/pymol-open-source.

[34] Carlo Adamo and Vincenzo Barone. "Toward reliable density functional methods without adjustable parameters: The PBE0 model". In: *The Journal of Chemical Physics* 110.13 (Apr. 1, 1999), pp. 6158–6170. DOI: 10.1063/1.478522. URL: https://doi.org/10.1063/1.478522.

[35] Stefan Grimme, Stephan Ehrlich, and Lars Goerigk. "Effect of the Damping Function in Dispersion Corrected Density Functional Theory". In: *Journal of Computational Chemistry* 32.7 (Mar. 1, 2011), pp. 1456–1465. DOI: 10.1002/jcc.21759. URL: https://doi.org/10.1002/jcc.21759.

[36] Heiner Schröder, Anne Creon, and Tobias Schwabe. "Reformulation of the D3(Becke–Johnson) Dispersion Correction without Resorting to Higher than C6 Dispersion Coefficients". In: *Journal of Chemical Theory and Computation* 11.7 (May 29, 2015), pp. 3163–3170. DOI: 10.1021/acs.jctc.5b00400. URL: https://doi.org/10.1021/acs.jctc.5b00400.

[37] Florian Weigend and Reinhart Ahlrichs. "Balanced Basis Sets of Split Valence, Triple Zeta Valence and Quadruple Zeta Valence Quality for H to Rn: Design and Assessment of Accuracy". In: *Physical Chemistry Chemical Physics* 7.18 (Jan. 1, 2005), p. 3297. DOI: 10.1039/b508541a. URL: https://doi.org/10.1039/b508541a.

[38] Florian Weigend. "Accurate Coulomb-Fitting Basis Sets for H to Rn". In: *Physical Chemistry Chemical Physics* 8.9 (Jan. 1, 2006), p. 1057. DOI: 10.1039/b515623h. URL: https://doi.org/10.1039/b515623h.

[39] Zoraida Freixa and Piet W. N. M. Van Leeuwen. "Bite Angle Effects in Diphosphine Metal Catalysts: Steric or Electronic?" In: *ChemInform* 34.41 (Sept. 19, 2003). DOI: 10.1002/chin.200341279. URL: https://doi.org/10.1002/chin.200341279.

[40] Lars A. Van Der Veen et al. "Origin of the Bite Angle Effect on Rhodium Diphosphine Catalyzed Hydroformylation". In: *Organometallics* 19.5 (Feb. 4, 2000), pp. 872–883. DOI: 10.1021/om990734o. URL: https://doi.org/10.1021/om990734o.

[41] Laura Falivene et al. "SambVca 2. A Web Tool for Analyzing Catalytic Pockets with Topographic Steric Maps". In: *Organometallics* 35.13 (June 27, 2016), pp. 2286–2293. DOI: 10.1021/acs.organomet.6b00371. URL: https://doi.org/10.1021/acs.organomet.6b00371.

[42] Boran Lee et al. "Exploring the Effect of Pincer Rigidity on Oxidative Addition Reactions with Cobalt(I) Complexes". In: *Organometallics* 42.8 (Apr. 5, 2023), pp. 708–718. DOI: 10.1021/acs.organomet.3c00079. URL: https://doi.org/10.1021/acs.organomet.3c00079.

[43] Elaine C. Meng et al. "UCSF ChimeraX: Tools for Structure Building and Analysis". In: *Protein Science* 32.11 (Sept. 29, 2023). DOI: 10.1002/pro.4792. URL: https://doi.org/10.1002/pro.4792.

[44] QChASM. *Buried Volume Tool*. Accessed: Friday 19th December, 2025. URL: https://github.com/QChASM/SEQCROW/wiki/Buried-Volume-Tool.

[45] Adarsh V. Kalikadien et al. "Unveiling the Impact of Ligand Configurations and Structural Fluxionality on Virtual Screening of Transition-Metal Complexes". In: *Digital Discovery* 4.8 (Jan. 1, 2025), pp. 2033–2044. DOI: 10.1039/d5dd00093a. URL: https://doi.org/10.1039/d5dd00093a.

[46] Dean M. Roddick. "Tuning of PCP Pincer Ligand Electronic and Steric Properties". In: *Topics in Organometallic Chemistry*. Aug. 22, 2012, pp. 49–88. DOI: 10.1007/978-3-642-31081-2_3. URL: https://doi.org/10.1007/978-3-642-31081-2_3.

[47] Wikipedia contributors. *Aromatic compound*. Accessed 2025-11-18. Oct. 7, 2025. URL: https://en.wikipedia.org/wiki/Aromatic_compound#:~:text=Aromatic%20compounds%20or%20arenes%20are,general%20chemical%20properties%20were%20understood..